Received: 4 July 2018 | Revised: 1 November 2018 | Accepted: 10 December 2018

DOI: 10.1111/bre.12331

ORIGINAL ARTICLE

WILEY Basin Research IAS EAGE

Fluid flow and pore pressure development throughout the evolution of a trough mouth fan, western Barents Sea

Jaume Llopart[1] | **Roger Urgeles**[1] | **Carl Fredrik Forsberg**[2] | **Angelo Camerlenghi**[3] | **Maarten Vanneste**[2] | **Michele Rebesco**[3] | **Renata Giulia Lucchi**[3] | **Denise Christina Rüther**[4] | **Hendrik Lantzsch**[5]

[1]Institut de Ciències del Mar (CSIC), Barcelona, Spain

[2]Norwegian Geotechnical Institute, Oslo, Norway

[3]Istituto Nazionale di Oceanografia e Geofisica Sperimentale (OGS), Trieste, Italy

[4]Western Norway University of Applied Sciences, Sogndal, Norway

[5]MARUM – Center for Marine Environmental Sciences and Faculty of Geosciences, University of Bremen, Bremen, Germany

Correspondence
Jaume Llopart, Institut de Ciències del Mar (CSIC), Barcelona, Spain.
Email: jaume.llopart@gmail.com

Funding information
DEGLABAR, Grant/Award Number: CTM2010-17386; CORIBAR-ES, Grant/Award Number: CTM2011-14807-E; SVAIS, Grant/Award Number: POL2006-07390; UNESCO, Grant/Award Number: IGCP-585; IUGS, Grant/Award Number: IGCP-640; PNRA, Grant/Award Number: 2013/B2.08 VALFLU

Abstract

Using a combination of geophysical and geotechnical data from Storfjorden Trough Mouth Fan off southern Svalbard, we investigate the hydrogeology of the continental margin and how this is affected by Quaternary glacial advances and retreats over the continental shelf. The geotechnical results show that plumites, deposited during the deglaciation, have high porosities, permeabilities and compressibilities with respect to glacigenic debris flows and tills. These results together with margin stratigraphic models obtained from seismic reflection data were used as input for numerical finite element models to understand focusing of interstitial fluids on glaciated continental margins. The modelled evolution of the Storfjorden TMF shows that tills formed on the shelf following the onset of glacial sedimentation (ca. 1.5 Ma) acted as aquitards and therefore played a significant role in decreasing the vertical fluid flow towards the sea floor and diverting it towards the slope. The model shows that high overpressure ratios (up to λ ca. 0.6) developed below the shelf edge and on the middle slope. A more detailed model for the last 220 kyrs accounting for ice loading during glacial maxima shows that the formation of these aquitards on the shelf focused fluid flow towards the most permeable plumite sediments on the slope. The less permeable glacigenic debris flows that were deposited during glacial maxima on the slope hinder fluid evacuation from plumites allowing high overpressure ratios (up to λ ca. 0.7) to develop in the shallowest plumite layers. These high overpressures likely persist to the Present and are a critical precondition for submarine slope failure.

1 | INTRODUCTION

Glacial troughs are the result of sediment erosion and minor till deposition by the ice sheets (Fiedler & Faleide, 1996). Ice stream bulldozing and sediment oversteepening at the shelf edge during glacial maxima, induce intense glacially derived mass wasting over the slope (Ó Cofaigh et al., 2013; Taylor, Dowdeswell, Kenyon, & Cofaigh, 2002; Vorren & Laberg, 1997). During glacial periods, ice streams provide a strong terrigenous input for the build-up of sedimentary fans located at the mouth of cross-shelf glacial troughs. These Trough Mouth Fans (TMFs) constitute the prominent areas of terrigenous sediment accumulation in high-latitude continental margins and induce shelf edge progradation, that may attain a few kilometres (Laberg & Vorren, 1996; Rebesco et al., 2011; Vorren, Lebesbye, & Larsen, 1990). Trough Mouth Fans are equivalent in size, volume and sediment mass allocation to deep-sea fans

located on mid- to low-latitude continental margins (Lucchi et al., 2013). Climatically modulated sedimentation in TMFs produces sedimentary sequences with alternating sediment types displaying large spatial variability, both vertically and horizontally (Llopart et al., 2015; Lucchi et al., 2013; Pedrosa et al., 2011). Trough Mouth Fans are characterised by uneven sedimentation rates (high during glacial maxima, low during the interglacials) (Laberg, Andreassen, Knies, Vorren, & Winsborrow, 2010) and contrasting sedimentary deposits, both in terms of facies (Lucchi et al., 2013) and physical properties (Llopart et al., 2014). High density and high shear strength glacigenic debris flows (GDF) are interbedded with low-density, low shear strength meltwater plume sediments (plumites) deposited during deglaciation periods (Hesse, Khodabakhsh, Klaucke, & Ryan, 1997; Landvik et al., 1998; Lucchi et al., 2012). During interglacial periods, hemipelagic sediment drapes, sedimentation by contour currents and dense shelf water-related turbidity currents may reshape the margin morphology (Ó Cofaigh et al., 2002). Although sediment deposition in TMFs is focused in extreme episodes during glacial maxima (GDFs) and deglaciations (plumites), TMFs contain nevertheless a rather continuous record of the interplay between past glacial dynamics and glaciomarine to marine sedimentary processes (Lucchi et al., 2013). Such temporal and spatial changes in ice and sedimentary load probably caused significant alterations in fluid flow circulation patterns in the TMF and adjacent outer shelf areas.

Highlights

- Geotechnical test show contrasting physical properties between glacial and glaciomarine sediments.
- The onset of glacial sedimentation (ca. 1.5 Ma) had a significant role in developing aquicludes on the shelf and diverting the fluid flow towards the slope.
- High resolution models show that undrained ice loading during Glacial Maxima had a major impact on the development of overpressures in shelf and shelf edge sediments.
- Rapid sedimentation of low-permeability sediments on the slope during Glacial Maxima hinder fluid flow release from glaciomarine sediments contributing to an overpressure increase.
- The mid to high overpressures developed within the glaciomarine sediments decrease their shear strength and bearing capacity becoming a first-order pre-conditioning factor for slope failures.

Fluid flow and excess pore pressure distribution patterns on continental margins have been modelled for both scientific and industrial purposes on mid-latitude continental margins

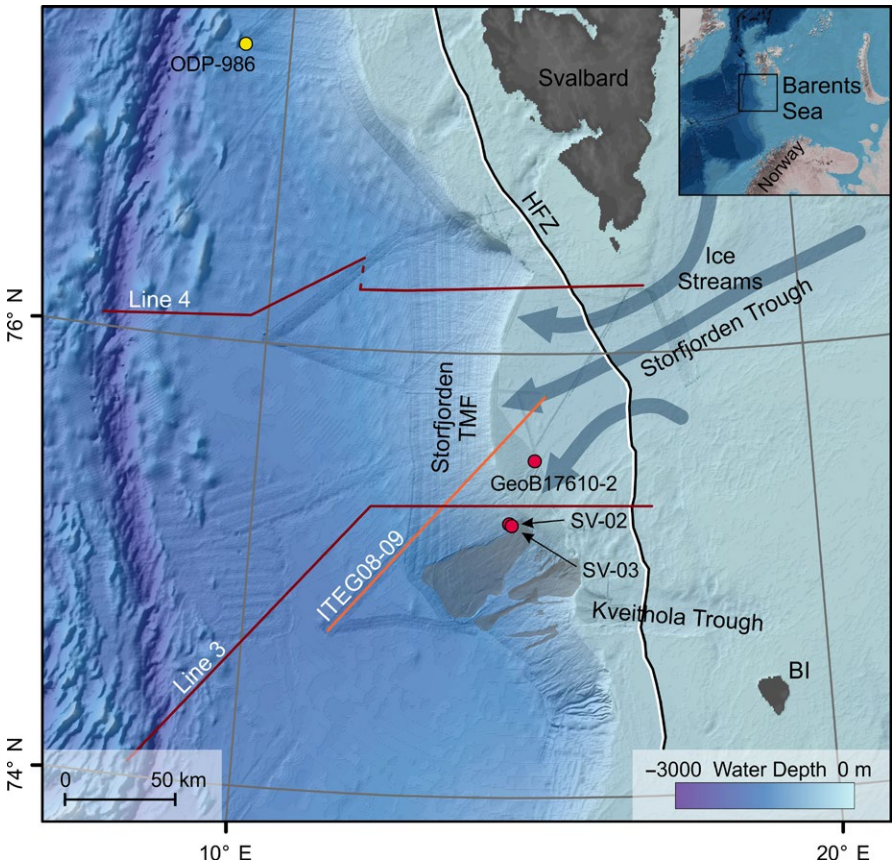

FIGURE 1 Study area and location of profile ITEG08-09 (orange) as well as lines 3 and 4 from Faleide et al. (1996) (dark-red) used for stratigraphic input to BASIN and Plaxis. Dots depict the location of cores collected during the SVAIS and CORIBAR cruises (red), and ODP site 986 (Raymo, Jansen, Blum, & Herbert, 2002) (yellow). Light grey shapes show Quaternary landslides identified in the area (Llopart et al., 2015), light blue arrows depict ice stream flows along Storfjorden Trough (Pedrosa et al., 2011). HFZ: Hornsund Fault Zone; BI: Bear Island

(e.g. Dugan & Sheahan, 2012; Gutierrez & Wangen, 2005; Javanshir, Riley, Duppenbecker, & Abdullayev, 2015; Kvalstad et al., 2005; Leynaud, Sultan, & Mienert, 2007; Marín-Moreno, Minshull, & Edwards, 2013; Stigall & Dugan, 2010; Urgeles et al., 2010). However, studies on high-latitude margins lack information on the combined effect of ice and sediment loading. In addition, previous studies are rather conceptual and do not consider the detailed stratigraphic patterns developed during individual glacial/interglacial cycles. The objective of this study was to investigate how the variability in sediment properties and loading history by ice and sediment affected the continental margin hydrogeology, the evolution of fluid flow patterns, the timing of overpressure build-up and how it impacted slope stability. To accomplish these objectives (a) we characterised the compression and permeability of glacial-deglacial-interglacial marine sediments, (b) we modelled the long-term margin evolution of the Storfjorden TMF (Figure 1) (from 2.7 Ma to Present) and (c) we carried out a second model of the last ca. 1 Myr at a higher resolution focused on the role of the shallower layers on the fluid flow and pressure evolution. A numerical model validation is performed in order to assess the accuracy of the results obtained.

2 | GEOLOGICAL SETTING

Formation of the western Barents Sea continental margin is linked to the gradual northward opening of the Norwegian-Greenland Sea, which began at the Paleocene-Eocene transition. The margin consists of three main provinces: (a) a southern sheared margin; (b) a central rifted complex associated with volcanism; and (c) a northern initially sheared and later rifted margin (Eldholm, Sundvor, Myhre, & Faleide, 1984; Faleide, Vdgnes, & Gudlaugsson, 1993; Talwani & Eldholm, 1977). The oceanic basement is overlain by prominent Plio-Quaternary prograding wedges, which resulted from a significant increase in sediment input (Sættem et al., 1994) after the onset of the major Northern Hemisphere Glaciations, at about 2.6–2.7 Ma (Butt, Elverhøi, Solheim, & Forsberg, 2000; Knies et al., 2009). Along the continental margin of the western Barents Sea three main sequences (GI–GIII) and eight regional seismic reflectors (R7-R1 and R4A) have been identified (Faleide et al., 1996; Knies et al., 2009) (Figure 2). R7 (base of GI) marks the onset of extensive glaciation 2.6–2.4 Ma ago off Svalbard and the Storfjorden Trough, while R4A, dated at ca. 1.3 Ma, is associated to the full development of shelf glacial troughs and TMFs (Rebesco et al., 2014). Reflectors R5 (1.5 Ma; base of GII) and R3 (0.78 Ma) mark the transition from net erosion to net accumulation in the outer shelf areas of Svalbard and Storfjorden respectively (Faleide et al., 1996; Hjelstuen, Elverhøi, & Faleide, 1996; Solheim, Andersen, Elverhøi, & Fiedler, 1996). The shallower GIII sequence above R1 has been described as a succession of glacial/interglacial periods (Laberg & Vorren, 1996).

During the Pleistocene, the development of TMFs, onset of glacigenic sedimentation, and major progradation are not synchronous in the Western Barents Sea (Dahlgren et al., 2005), as glaciers reached the shelf break in the southwestern

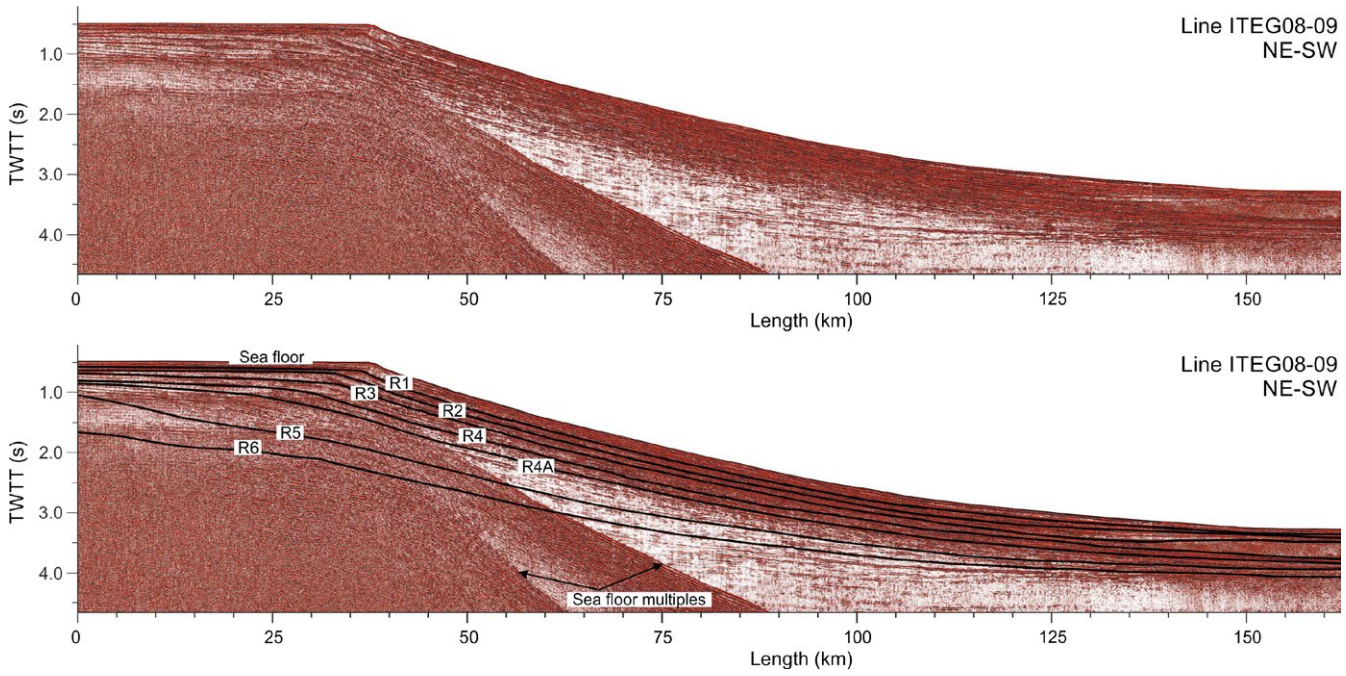

FIGURE 2 Top: Seismic profile ITEG08-09 used for basin analysis in BASIN and Plaxis. Bottom: Profile ITEG08-09 with regional reflectors R6 to R1 highlighted

Barents Sea not earlier than 1.0 Ma, while in the Spitsbergen area was around 1.6 Ma (Butt et al., 2000; Forsberg, Solheim, Jansen, & Andersen, 1999). In the western Barents Sea, continental margin large volumes of glacial sediments deposited at sedimentation rates of 0.25–0.62 m/kyr, with recorded peaks of 1.96–6.9 m/kyr (Hjelstuen et al., 1996; Llopart et al., 2015; Pedrosa et al., 2011) in the Storfjorden TMF, and contributed to the rapid build-up of the fans during glacial maxima periods.

The present Barents/Svalbard margin can be divided into three sedimentary belts: (a) the continental shelf mainly composed of basal deformation tills and grounding zone wedges, (b) the shelf edge and upper/middle slope made of till deltas that formed at the grounding-line and interbedded with ice rafted detritus (IRD), debris flows, hemipelagic sediments and turbidites that originated from subglacial meltwater plumes and (c) the lower slope and abyssal plain, which are made of distal turbidity currents, hemipelagic sediments, contourites and IRD (Dowdeswell, Elverhøi, & Spielhagen, 1998; Ó Cofaigh, Taylor, Dowdeswell, & Pudsey, 2003; Rebesco et al., 2013; Stein, 2008). Several slope failures with volumes spanning at least seven orders of magnitude (10^{-2}–10^{5} km^{3}) disrupt the slope stratigraphy throughout the western Barents Sea margin (e.g. Llopart et al., 2015; Pedrosa et al., 2011; Rebesco et al., 2012).

3 | DATA AND METHODS

3.1 | Geophysical and geotechnical data

The data used in this study were collected during three coordinated research cruises within the International Polar Year Activity 367: *BIO Hespérides* cruise SVAIS (2007), R/V *OGS-Explora* cruise EGLACOM (2008) and *R/V Maria S. Merian* MSM30 cruise CORIBAR (2013) (Figure 1). The profile used for basin modelling in this study corresponds to the multi-channel seismic reflection profile ITEG08-09 acquired during the EGLACOM cruise. This profile was acquired using a 160 cubic inches array of four sleeve air guns and a 1,200 m digital streamer with 96 channels spaced 12.5 m. Recording was performed at a sampling rate of 1 ms. Processing at OGS using the Paradigm ECHOS software included a *t*-squared scaling for spherical divergence correction, multi-channel shot spiking deconvolution, bandpass filtering following the water bottom and trace equalisation (Rebesco et al., 2011).

Consolidation and permeability tests were performed on nine samples from cores SV-02, SV-03 (SVAIS cruise) and GeoB17610-2 (CORIBAR cruise) (see Supporting Information Figure S1). Stepped loading consolidation tests were carried out using a GDS Rowe & Barden-type Consolidation cell equipped with three 2 MPa pressure/volume controllers. The tests have been performed according to the British Standard Methods for soil testing (British Standards Institution, 1990). After each consolidation step, permeability was measured by inducing a pressure gradient of 10 kPa between both ends of the specimen. The water volume that circulated through the sample at a given time interval allowed to determine the permeability using Darcy's law.

Consolidation and permeability tests provide the input parameters used for hydrogeological modelling. These parameters include initial porosity (ϕ_0), initial hydraulic conductivity (k_0) and initial specific storage (S_0). Previous studies in the area (e.g. Llopart et al., 2015; Lucchi et al., 2010; Rebesco, Camerlenghi, & Llopart, 2015), indicate that the main sediment types involved on high-latitude continental margins such as that of the western Barents Sea are turbidites (including plumites on the shallower parts of the slope), GDFs, tills and hemipelagic sediments. However, we could not sample hemipelagic sediments for consolidation testing. Parameters for hydrogeological modelling for hemipelagic sediments are therefore taken from the literature.

3.2 | Stratigraphic model

Seismic reflection data provide the required input geometry (interfaces between major sedimentation packages) for hydrogeological modelling. The regional reflectors R6 to R1, described in Faleide et al. (1996), were identified in seismic reflection profiles (see Llopart et al. (2015) for full seismic reflection profiles network) and tied to ODP Site 986 data (Forsberg et al., 1999). Reflector R7 and the top of the oceanic basement (OB) were constrained in the models with information from two higher penetration seismic lines north (4) and south (3) of Storfjorden (Faleide et al., 1996) as the data set collected during the three cruises did not have enough penetration to image these reflectors (Figure 2). The velocities for time to depth conversion of the picked horizons are based on a linear p-wave seismic velocity gradient of $1.48 + 1.5z$ km/s, where z is depth in the sedimentary section in seconds. This gradient is consistent with sonic velocity data from ODP Site 986D (Laberg, Forwick, & Husum, 1996; Figure 1). The resulting velocities of ca. 3 km/s at the base of the sedimentary section are in agreement with refraction and wide-angle reflection data (Hjelstuen et al., 1996). Units between the oceanic basement and the seafloor have been named U1 to U8 from top to bottom. Unit U1, above reflector R1, was subdivided in subunits G to A_1, which correspond to the shallow stratigraphic units identified by Llopart et al. (2015) (Table 1). Facies spatial variation is based on the acoustic facies mapping from sub-bottom profiler data of Llopart et al. (2015) and adjusted to the shelf break position below reflector R1, where sub-bottom profiles provide no information.

Ages of reflectors R7 to R1 were selected according to Knies et al. (2009). Above reflector R1, the chronological framework was previously established by Llopart et al.

TABLE 1 Age of the horizon, units and their lithology used as input for hydrogeological modelling

Sequence	Unit	Subunit	Lithology	Horizon	Age (ka)
				Seafloor	0
GIII	U1	A_1	Hemipelagic sediments	Base A_1	13*
		A_2	Plumites grading to hemipelagic sediments	Base A_2	19.5*
		B	Tills grading to GDFs and hemipelagic sediments	Base B	22.5*
		C	Plumites grading to hemipelagic sediments	Base C	60*
		D	Tills grading to GDFs and hemipelagic sediments	Base D	64*
		E	Plumites grading to hemipelagic sediments	Base E	135*
		F	Tills grading to GDFs and hemipelagic sediments	Base F	167*
		G	Plumites grading to hemipelagic sediments	Base G (R1)	220*
GII	U2		Tills grading to GDFs, plumites and hemipelagic sediments	R2	500#
	U3		Tills grading to GDFs, plumites and hemipelagic sediments	R3	780#
	U4		Tills grading to GDFs, plumites and hemipelagic sediments	R4	990#
	U4A		Tills grading to GDFs, plumites and hemipelagic sediments	R4A	1200#
	U5		Mixed GDFs and plumites grading to plumites and hemipelagic sediments	R5	1500#
GI	U6		Plumites grading to hemipelagic sediments	R6	1650#
	U7		Plumites grading to hemipelagic sediments	R7	2700#
G0	U8		Mixed turbidites and hemipelagic sediments grading to hemipelagic sediments	OB	3500#

*: (Llopart et al., 2015), #: (Knies et al., 2009).

[a]Llopart et al. (2015). [b]Knies et al. (2009).

(2015) (Table 1). In agreement with the information from Forsberg et al. (1999), we considered that R7 marks the transition from purely hemipelagic sediments (below) to mixed plumites and hemipelagic sedimentary facies. Uncertainties in sediment type distribution prevent a better characterisation of this interval, but the sedimentary facies are consistent with a relatively distal position on a glacially influenced prograding continental margin. At the onset of the Northern Hemisphere Glaciation (NHG) a transition from turbidites to GDFs in the north-eastern part occurred (units R7 to R6). The enhanced glacial conditions from unit R5, roughly corresponding to the onset of the NHG, greatly contributed to the shelf edge progradation, deposition of tills on the shelf and the build-up of GDF lenses on the slope(Knies et al., 2009). From R1 time (220 ka) to present day, the models have higher chronologic resolution and display alternation of glacial and interglacial cycles depicted by cyclic deposition of GDFs and plumites on the slope.

3.3 | Continental margin hydrogeological modelling

The hydrogeological evolution of the Storfjorden Trough Mouth Fan has been modelled from its initial growth (2.7 Ma) to present using two different software. BASIN (Bitzer, 1996, 1999) models focused on understanding the long-term evolution of the margin since 2.7 Ma, while Plaxis (PLAXIS bv, 2015) was used to model the last 220 kyrs. BASIN is limited in the number of sediment types (up to four) and in the maximum number of elements in the horizontal direction (40). In contrast, Plaxis allows a higher computational load, although there are restrictions to the size of the model (i.e. number of cells) that can be implemented. The hydrogeological models presented in this study do not consider hydrocarbon generation, the presence of free gas or gas hydrates. Only water single-phase flow is considered. Supporting this assumption, no evidences of fluid venting (i.e. gas mud or oil) or gas hydrates have been found in the Storfjorden and Kveithola TMFs (Llopart et al., 2015; Pedrosa et al., 2011; Rebesco et al., 2014).

3.3.1 | Finite element hydrogeological modelling with BASIN

The Finite Element Software BASIN (Bitzer, 1996, 1999) has been used to carry out the long-term hydrogeological evolution of the Storfjorden continental margin and to simulate fluid migration and pore pressure development. BASIN (Bitzer, 1996, 1999) is based on a forward modelling approach. For a given set of initial and boundary geological

conditions the sedimentary basin evolution is calculated. Compaction and fluid flow are coupled through the consolidation equation and the nonlinear form of the equation of state for porosity, allowing nonequilibrium compaction and overpressure to be calculated (Bitzer, 1999). Instead of empirical porosity-effective stress equations, a physically consistent consolidation model is applied which incorporates porosity-dependent sediment compressibility (Equation 1).

$$(\partial/\partial x)\left(k_{x(\emptyset)}\,\partial p/\partial x\right)+(\partial/\partial x)\left(k_{z(\emptyset)}\,\partial p/\partial z\right) = \left(1-\emptyset\right)\rho g\alpha_{(\emptyset)}\,\partial p/\partial t \quad (1)$$

where $k_{x(\phi)}$ is the porosity-dependent hydraulic conductivity in the x-direction, $\alpha_{(\phi)}$ is the porosity-dependent sediment compressibility, p the fluid pressure, ϕ the porosity, ρ is the sediment bulk density and g is the gravity constant.

Sediment compressibility in BASIN is calculated from the specific storage (S_s) using Equation 2:

$$S_s=\rho g\alpha \quad (2)$$

where α is the sediment compressibility. The rate of pore pressure generation thus depends on stratigraphic architecture, sedimentation rate, sediment compressibility and permeability.

BASIN (Bitzer, 1996, 1999) allows input properties for a maximum of four sediment types. However, these four sediment types can be mixed within and along a particular unit simulating gradual facies changes. Physical properties where sediment types are mixed are averaged according to the relative sediment composition. Erosion or sediment unloading is not suitably simulated within BASIN. The total length of the modelled transect in Basin (along seismic profile ITEG08-09) is around 156 km (Figures 1 and 2). The left and right model boundaries are constrained so that neither horizontal displacement nor fluid flow is allowed. The bottom boundary of the model is vertically and horizontally fixed.

In order to visualise the model evolution through time, parameters are logged along synthetic wells placed at 20 km (shelf), 36 km (present-day shelf break), 42 km (upper slope) and 80 km (middle slope).

3.3.2 | Finite element hydrogeological modelling with PLAXIS

With the aim to investigate the Late Quaternary hydrogeological evolution of the Storfjorden TMF in higher detail and to account for the effect of ice loading and unloading during glaciations and deglaciations respectively, the PLAXIS 2015 software package (PLAXIS bv, 2015) has been used. Within PLAXIS, the Soft Soil constitutive model was selected, according to the characteristics of the sediment types present in the study area and the nature of the problem to be modelled. The Soft Soil constitutive model is a Cam-clay-type model especially meant for primary compression of near normally consolidated clay-type soils. Features of interest in the soft-soil model for this study are: stress-dependent stiffness, memory for pre-consolidation stress and distinction between primary loading and unloading-reloading (Plaxis bv, 2015). In order to analyse the simultaneous pore pressure development and deformations during sediment deposition (Equations 3 and 4), a fully coupled flow-deformation analysis calculation was selected. This coupled analysis is represented by both the equilibrium and continuity equations of the water-soil mixture, which are simultaneously solved (Equations 3 and 4):

$$d\bar{\sigma}'=Md\bar{\varepsilon} \quad (3)$$

$$\begin{bmatrix} K & Q \\ 0 & -H \end{bmatrix}\begin{bmatrix} \bar{v} \\ \bar{p}_w \end{bmatrix}+\begin{bmatrix} 0 & 0 \\ C & -S \end{bmatrix}\begin{bmatrix} \frac{\mathrm{d}\bar{v}}{\mathrm{d}t} \\ \frac{\mathrm{d}\bar{p}_w}{\mathrm{d}t} \end{bmatrix}=\begin{bmatrix} \bar{f}_u \\ G+q_p \end{bmatrix} \quad (4)$$

where $\bar{\sigma}'$ is the effective stress vector, M is the material stress-strain matrix, ε' is the strain vector, K is the stiffness matrix, Q and C are coupling matrices, H is the permeability matrix, $\bar{v}$ is the displacement vector, $\bar{p}_w$ is the pore pressure vector, S is the compressibility matrix, $\bar{f}_u$ is the load vector in an element, G is the flow gravity vector in the y-direction and $\bar{q}_p$ is the flux on the element boundaries.

The main input parameters for the Soft Soil model are the modified compression index (λ^*), modified swelling index (κ^*), effective cohesion (c'), friction angle (φ) and void ratio (e). Modified indexes are related to the one-dimensional compression C_c and swelling C_s indexes derived from the oedometer test and the void ratio following Equations 5 and 6. Groundwater flow is calculated assuming fully saturated conditions. The input parameters are the vertical and horizontal hydraulic conductivities (k_y and k_x), as well as the permeability change (c_k) with the void ratio variation due to consolidation (Equation 7).

$$\lambda^*=\frac{C_C}{2.3\,(1+e)} \quad (5)$$

$$\kappa^*=\frac{C_s}{2.3\,(1+e)} \quad (6)$$

$$log\left(\frac{k}{k_0}\right)=\frac{\Delta e}{c_k} \quad (7)$$

To guarantee the computation stability while increasing the resolution of the Finite Elements Mesh (FEM) and therefore of the output results, the model has been restricted to the mid- and outer shelf and proximal slope down to 2,200 mbsl, where the largest variations occur in both sediment type and loading characteristics. By shortening the model, we intend to generate a mesh of a manageable size, given the increase in

resolution, while minimising calculation errors and improving convergence stability. The model is ca. 43,500 15-node elements with widths between 150 m in the deeper layers and 5 m in the shallower ones.

Time intervals are the same as those of the BASIN model. The left and right model boundaries are constraint so that neither horizontal displacement nor fluid flow is allowed. The bottom boundary of the model is vertically and horizontally fixed.

To account for compaction-derived fluid flow of the sedimentary sequences below those upper 2,200 m of sediment, a time-dependent flow boundary condition has been set. The magnitude of the flow along this surface is taken from the BASIN model throughout deposition from R4A to present at the depth of R4A. Not accounting for the fluid compaction driven flow from deeper sediments would lead to underestimated pore pressures and overpressure ratio. Horizon R4A in the PLAXIS model is set to its present day position on the margin.

To understand the influence of ice loading on continental margin hydrogeology, two sets of simulations were carried out: one set that accounts for such ice loading and another set that does not include the ice loads. To simulate ice loading in PLAXIS, an incremental vertical load has been applied along the shelf area during the onset of glaciation and has been set constant during glacial maxima. The ice load corresponds to the ice (h_i) thickness above sea level minus the emerged ice thickness necessary to counter the buoyancy effect.

$$h_i = \frac{\rho_w h_w}{\rho_i} + z \tag{8}$$

where h_i and h_w are the ice thickness and water depth respectively, ρ_w and ρ_i are sea water and ice densities and z is the ice height above sea level to balance ice buoyancy. In our simulations, the ice thickness above sea level necessary to counter ice buoyancy is 120 m in the inner shelf (left limit of the model) and 100 m on the outer shelf (close to the shelf edge). The total simulated ice thickness above sea level is therefore 190 m and 150 m on the inner and outer shelf respectively, which is in agreement with models by Dowdeswell and Siegert (1999) and Svendsen et al. (2004). Due to thinning of the ice sheet towards the ice edge (shelf edge during glacial maximum) the applied ice load is higher in the inner shelf than in the outer shelf. Further, during ice retreat the applied ice load has been set as decreasing through time. Water depths are extracted from the bathymetric data and account for a ca. 105 m sea level lowstand during glacial maxima (Rohling et al., 2014). At the shelf edge, the maximum water depth is estimated to be 290 m during glacial maxima. The PLAXIS simulations that included the effects of ice loading over the continental shelf assumed that the ice is an impervious material and as such the ice-sediment interface is considered an undrained boundary in agreement with models of ice sheet dynamics (Tulaczyk, Kamb, & Engelhardt, 2000). Within an ice-sheet there are cavities and channels that allow for some drainage through this interface (Kyrke-Smith, Katz, & Fowler, 2013), but evidence of high-water pressure beneath ice sheets (Engelhardt & Kamb, 1997) suggests that the undrained assumption is acceptable for the proposed modelling.

In this study, pore pressure is described in terms of overpressure ratio (λ) as defined by Flemings et al. (2008) as:

$$\lambda = (p - P_h)/(\sigma_v - P_h) \tag{9}$$

where p is the pore pressure, P_h is the hydrostatic pressure and σ_v is the lithostatic or total stress.

The initial thickness (H_i) of different strata used as input for the models was calculated using van Hinte's decompaction equation (Van Hinte, 1978):

$$H_i = H_f[(1-\phi_f)/(1-\phi_0)] \tag{10}$$

TABLE 2 Most important parameters derived from consolidation/permeability tests in this study. GDF: Glacigenic Debris Flows, e_0: initial void ratio at 1 kPa (void ratio of tills has been taken at σ_c, in brackets the e_0 at 1 kPa), k_0: initial hydraulic conductivity, S_0: initial specific storage, σ_c: pre-consolidation pressure, OCR: Over-consolidation Ratio, C_c: compressibility index, C_s: swelling index

	Sediment type	e_0	k_0 (m/s)	S_0 (m^{-1})	σ_c (kPa)	*OCR*	C_c	C_s
SV02-02	Plumites	1.48	2.3E-09	0.024	18	1.0	0.33	0.062
SV02-03	Plumites	1.89	5.5E-09	0.019	32	1.1	0.41	0.066
SV02-04	Plumites	1.72	7.2E-09	0.032	44	1.0	0.38	0.043
SV03-04	Plumites	1.83	4.2E-08	0.023	42	1.0	0.37	0.058
SV03-06	Plumites	1.24	1.0E-09	0.021	59	1.0	0.24	0.029
SV02-05	GDF	1.04	3.6E-10	0.009	65	1.2	0.27	0.022
SV02-06	GDF	0.92	1.1E-09	0.007	73	1.1	0.20	0.026
GeoB17610-2-319	Tills	0.94 (1.38)	4.9E-10	0.006	58	1.5	0.22	0.012
GeoB17610-2-330	Tills	0.93 (1.29)	3.2E-10	0.004	57	1.5	0.20	0.027

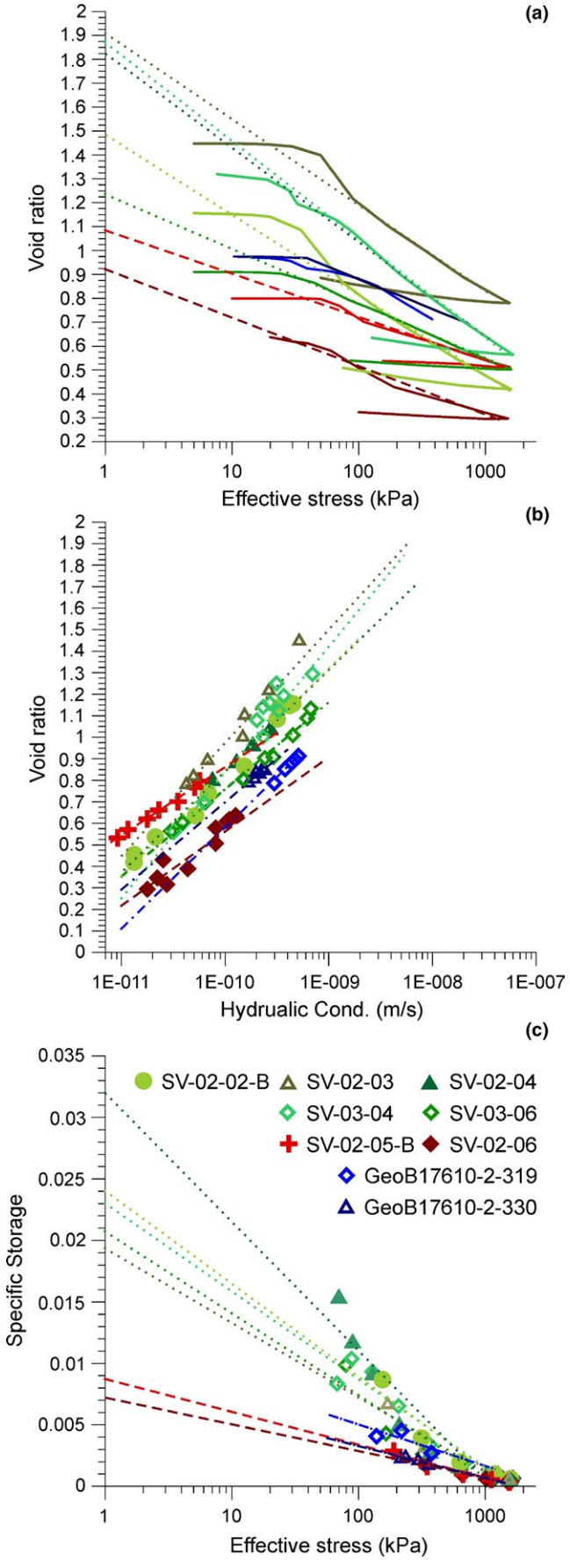

FIGURE 3 Consolidation/permeability test results: (a) effective stress versus void ratio for the tested samples, (b) flow-through permeability versus void ratio, (c) effective stress versus specific storage. Dashed/dashdotted/dotted lines show extrapolation to 1 kPa used to determine initial (depositional) parameters. For till samples, the initial parameters are calculated at the pre-consolidation stress. Dotted lines in shades of green correspond to tests in plumite samples, dashed lines in shades of red to tests in GDFs, and dashdotted lines in shades of blue to tests in tills

where ϕ_0 is the initial porosity at deposition, ϕ_f is the present-day porosity and H_f is the present-day sediment thickness.

4 | RESULTS

4.1 | Sediment compressibility and permeability characteristics

Consolidation and permeability testing were performed on specimens from three sediment types previously interpreted by Llopart et al. (2015) and Lucchi et al. (2013) as: (a) laminated sediments (meltwater plumites), (b) chaotic slope sediments (GDFs) and (c) chaotic shelf sediments (tills) (Table 2 and Supporting Information Figure S1).

The void ratio determined for plumites samples varies between 1.1 and 1.5, while GDFs show lower values that range between 0.6 and 0.8. Estimated mean void ratios at deposition e_0 ($\sigma' = 1$ kPa) are 1.73 and 0.98 respectively (Table 2 and Figure 3). These latter values have been calculated using logarithmic regression of the virgin consolidation line for each sediment sample. Because the deposition process of tills occurs under the influence of the ice load, e_0 has been calculated at the pre-consolidation pressure (σ'_{pre}) with a mean value of 0.93. In general terms, in situ hydraulic conductivities (k) are low (10^{-10}-10^{-8} m/s). The mean initial hydraulic conductivities for plumites, GDFs and tills are 1.1×10^{-8} m/s, 7.3×10^{-10} m/s and 4.0×10^{-10} m/s respectively (Table 3). In turn, mean values of initial specific storage are 0.024, 0.008 and 0.005, calculated at $\sigma' = 1$ kPa for plumites and GDFs, and σ'_{pre} for tills. The specific storage and hydraulic conductivities show also a more marked decrease with increasing stress in plumites than in GDFs or tills (Figure 3). Initial values are used hereinafter as depositional values. The slope of the virgin consolidation line (compression index; C_c) for plumites is also steeper than that of GDF and tills with mean values of 0.35 for plumites, 0.23 for GDFs and 0.21 for tills. C_s values are 0.052, 0.024 and 0.02 respectively (Figure 3).

The consolidation tests performed in this study clearly show that climatically controlled sedimentation produces sediments with contrasting physical properties. In this case, samples SV02-02, SV02-03, SV02-04, SV03-04 and SV03-06,

TABLE 3 Parameters used for hydrogeological modelling. (1) this study. (2) Raymo et al. (1999). (3) Urgeles et al. (2010). ϕ_0: initial porosity, S_0: initial specific storage, k_0: initial hydraulic conductivity, ρ_g: grain density, θ: tortuosity ($\theta = \sqrt{1 - \ln(\phi^2)}$, Boudreau, 1996)

	Plumites	GDFs	Till	Hemipelagic sediments
ϕ_0	0.63(1)	0.49(1)	0.48(1)	0.77(2)
S_0 (m^{-1})	0.025(1)	0.008(1)	0.004(1)	0.044(2)
k_0 (m/s)	5.1E-9(1)	7.2E-10(1)	5.0E-10(1)	3.0E-9(3)
ρ_g (kg/m^3)	2650	2650	2650	2650
θ	1.4	1.5	1.5	1.2

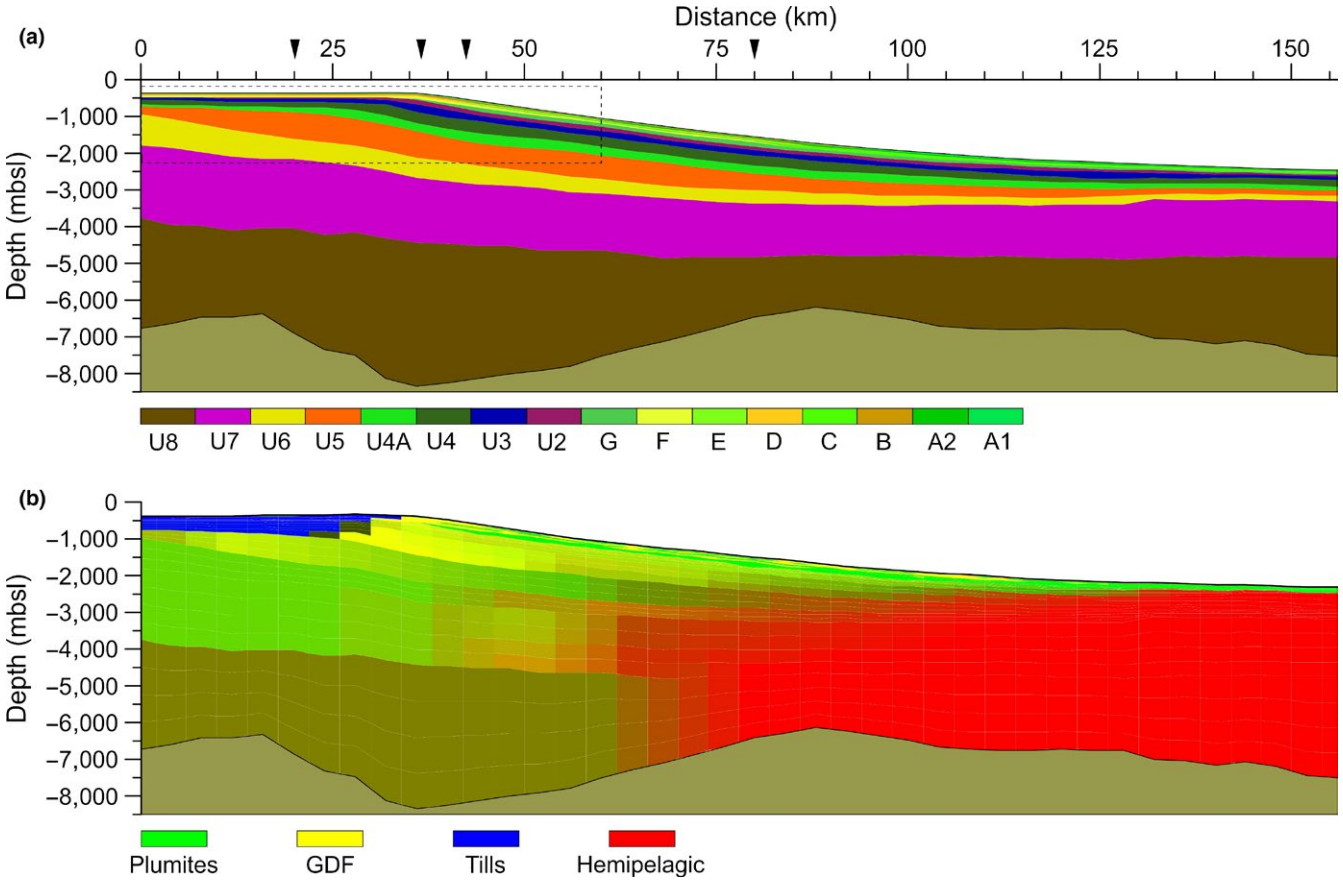

FIGURE 4 Margin stratigraphy of the Storfjorden TMF (a) and facies distribution (b) at Present day used for modelling with BASIN. For key to Units see Table 1. Vertical exaggeration 5:1. Dashed box depicts area modelled with Plaxis. Black arrows mark the location of the synthetic wells. OB: Oceanic Basement; GDF: Glacigenic Debris Flows

corresponding to the meltwater plumites, are more porous, permeable and have higher compressibility than samples SV02-05 and SV02-06, corresponding to GDF sediments. These differences are partially controlled by differences in consolidation stress, but trends in the slope of the virgin consolidation line and values derived at deposition ($\sigma' = 1$ kPa) indicate that the differences are genuine. Plumites are finer grained and better sorted than GDFs (see Lucchi et al., 2013), which are probably at the origin of the observed differences in physical properties. Plumites also have higher water content and lower shear strength compared to GDFs at the same consolidation stress (see Supporting Information Figure S1). Pre-consolidation pressures indicate normally consolidated sediments for both plumites and GDFs. Conversely, the pre-consolidation effective stress of till samples compared to the in situ effective vertical stress (assuming hydrostatic conditions) shows an Over-Consolidation Ratio (OCR) of ca. 1.5.

Pre-consolidation pressures from these shallow till samples, involve an ice load around 60 kPa, corresponding to ca. 6 m of ice above the buoyancy compensation thickness. The low pre-consolidation pressures of these tills probably result from their deposition right at the beginning of the deglaciation or in an ice frontal position (till delta). Alternatively, the low pre-consolidation pressures can be explained if the

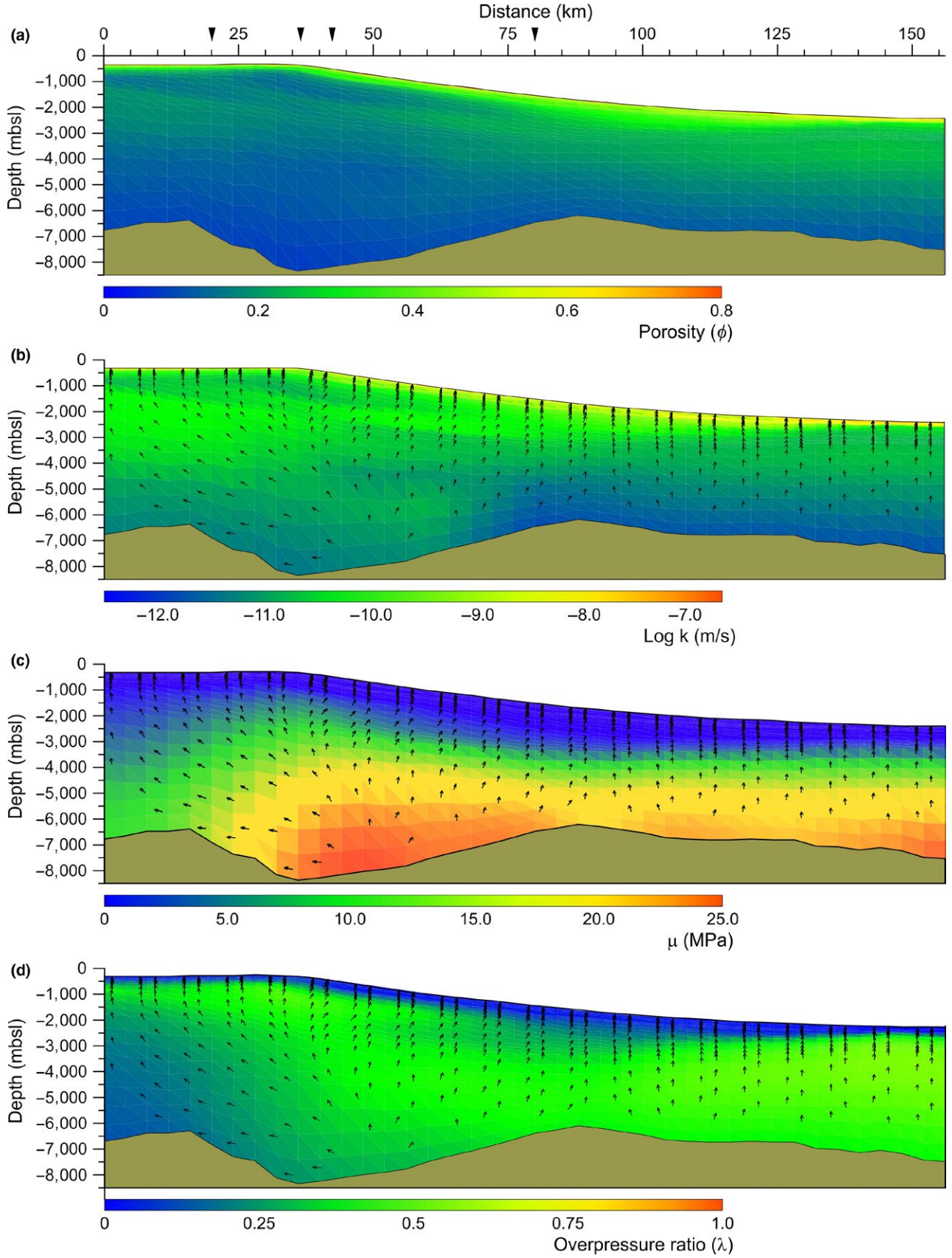

FIGURE 5 (a) Output of BASIN simulation at Present day for the Storfjorden TMF: (a) fractional porosity, (b) log hydraulic conductivity (m/s), (c) Excess pore pressure (MPa) and (d) Overpressure ratio (λ).Vertical exaggeration 5:1. Black arrows on top scale mark the location of the synthetic wells. See supporting information Video S1 for the complete simulation

ice sheet was warm-based, that is, if significant overpressure existed within the till sediments due to loading by an impervious ice sheet. Such conditions would favour a highly mobile ice sheet and a deformable till base (Christoffersen & Tulaczyk, 2003). The depositional values derived from the geotechnical test used in the hydrogeological models are summarised in Table 3.

4.2 | Hydrogeological models

Two models have been implemented to understand the hydrogeological evolution of Storfjorden TMF. The combined use of the two models provides complementary information: BASIN is adequate to investigate the thick sedimentary sequences deposited during its long-term evolution, whereas PLAXIS is more suitable for more detailed studies. The BASIN output also supplies the boundary conditions (i.e. basal fluid flow) for the PLAXIS model. These boundary conditions are mandatory while modelling the evolution of the shallower most part of a continental margin.

4.2.1 | Continental margin long-term hydrogeological evolution

Model results with BASIN (Bitzer, 1996, 1999) show that sediment characteristics at deposition have a major effect on the subsequent evolution of porosity and permeability, which are controlled by consolidation due to the overburden. The outcome of the model at the present-day stage in the deep-water areas of the margin shows porosities that are consistent with those recorded at ODP Site 986 (Jansen, Raymo, Blum, & Al, 1996). In this final stage of the model, porosities higher than 0.4 are present only at shallow depths where the overburden is lower than 1 MPa (Figure 5a). However, on the shelf and upper slope a low porosity (below 0.15) wedge develops, which corresponds to the area where tills and GDFs are the prevailing sediments (Figure 4b). Below the shelf and upper slope, the modelled hydraulic conductivities are lower than in the adjacent middle and lower slope where plumite and hemipelagic sedimentation predominates. Values of hydraulic conductivities higher than 10^{-9} m/s (Figure 5b) are only found in the first metres below the seafloor or in the distal part of the margin, where plumite and hemipelagic sedimentation are dominant (Figure 4b).

Fluid flow is mainly vertical along the entire margin, which indicates that sediment self-weight consolidation is the main factor driving fluid flow along the margin (Figure 5b). This vertical flow pattern is however modified near the major depocentre (between kilometres 30 and 50 in the modelled profile). In addition, close to the shelf edge, the fluid is diverted to the upper slope. Such diversion is likely due to the low hydraulic conductivity of till sediments present along the shelf (Figure 5b).

Sediment physical properties, stratigraphic architecture and sedimentation rates control excess pore pressure evolution. Pliocene sedimentation above the oceanic basement (below reflector R7) spanned ca. 3.2 Myrs, and at the end of deposition of sequence G0, excess pore pressures remain below 3 MPa along most of the margin. Only where the sedimentary cover was thickest (depocentre located between 30 and 40 km in the modelled transect with mean sedimentation rates up to 19 kg m^{-2} yr^{-1}), excess pore pressures reached 7 MPa (Figure 6c,e). From 2.7 to 1.5 Ma (sequence GI), excess pore pressures increased all along the margin with higher values in the left half of the model coinciding with the depocentre that already developed during deposition of the previous stage (Figure 6c). In this area, excess pore pressures reach 25 MPa, while overpressure ratios increased from ca. 0.1 to 0.2 at the shelf and 0.3 off the shelf edge. However, the shallower thousand metres of the entire margin show values below 0.1.

Overpressure ratios started to increase significantly at relatively shallow depths (above 1,000–1,500 mbsf) with deposition of unit U4 (ca. 990 ka), when glaciers deposited significant till layers on the shelf (NE part of the model; Figure 4). The accumulation of low-permeability marine sediments at relatively high sedimentation rates of up to 45.7 kg m^{-2} yr^{-1} (particularly after onset of glacial sedimentation on the shelf and upper slope), has a clear impact on excess pore pressure build-up and the pattern of fluid flow that develops on the continental margin. From 780 ka (age of reflector R3) to Present, overpressure ratios along the shelf to middle slope sharply increased at shallow depths (above 1,500 mbsf) with values up to 0.4, whereas in the distal part of the margin the increase was not that significant (Figure 6). The predominantly low porosity and permeability sediments (tills and GDFs) and the low lithostatic stress at shallow depths along the shelf are responsible for the increase in overpressure in that most proximal area (Figure 6c,e).

After burial by ca. 1,500 m of younger sediment, porosity and hydraulic conductivities of all sediments attain relatively low values ranging from 0.08–0.2 to 10^{-11}–10^{-9}, respectively, in most of the model domain. During deposition of the GIII sequence (last ca. 220 kyrs), deposition of glacial units F, D and B, involved a significant increase in overpressure ratio in the shallower sediments (above 300 mbsf), whereas during deposition of deglacial and interglacial sediments overpressures decreased. Elevated overpressure ratios developed at the shelf edge/upper slope and middle slope areas with overpressure ratio values up to 0.6 (Figure 6b,d,f). At the end of the Last Glacial Maximum most of the margin is dominated by overpressure ratios ranging between 0.4 and 0.6. In the first 100 metres below the sea floor, overpressure ratios are mostly in the range of 0.35–0.45, and only near the shelf edge area, overpressure ratios reached values ca. 0.58 at shallow depths.

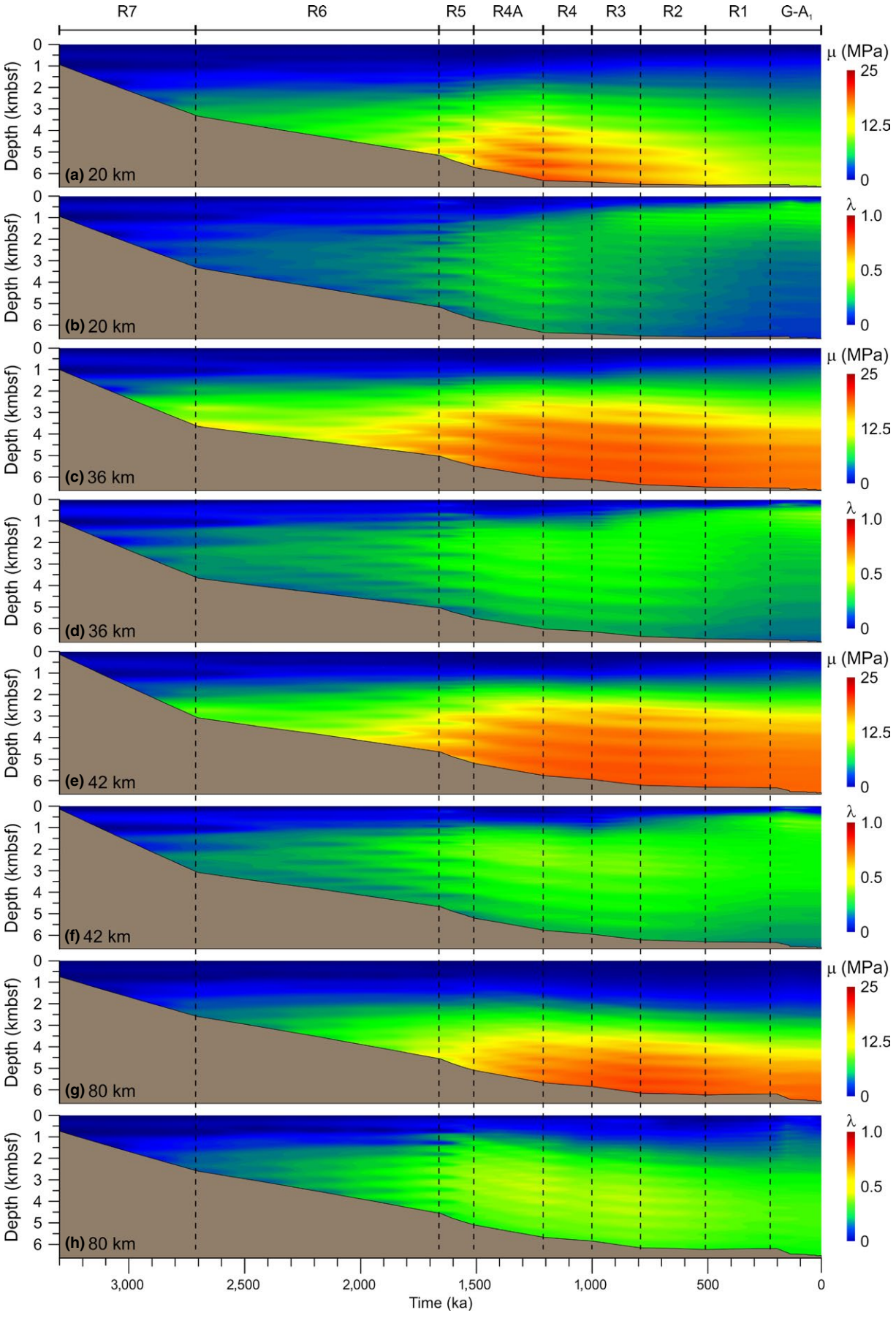
R7
R6
R5
R4A
R4
R3
R2
R1
G-A1
Depth (kmbsf)
μ (MPa)
λ
(a) 20 km
(b) 20 km
(c) 36 km
(d) 36 km
(e) 42 km
(f) 42 km
(g) 80 km
(h) 80 km
Time (ka)
3,000
2,500
2,000
1,500
1,000
500
0

FIGURE 6 Time vs depth evolution of excess pore pressures (MPa) (a, c, e and g) and overpressure ratio (λ) (b, d, f and h) at the synthetic observation wells located at 20 (shelf), 36 (shelf edge), 42 km (upper slope) and 80 km (lower slope) along the model (see Figure 5 for location). Note the banding due to interpolation artifacts

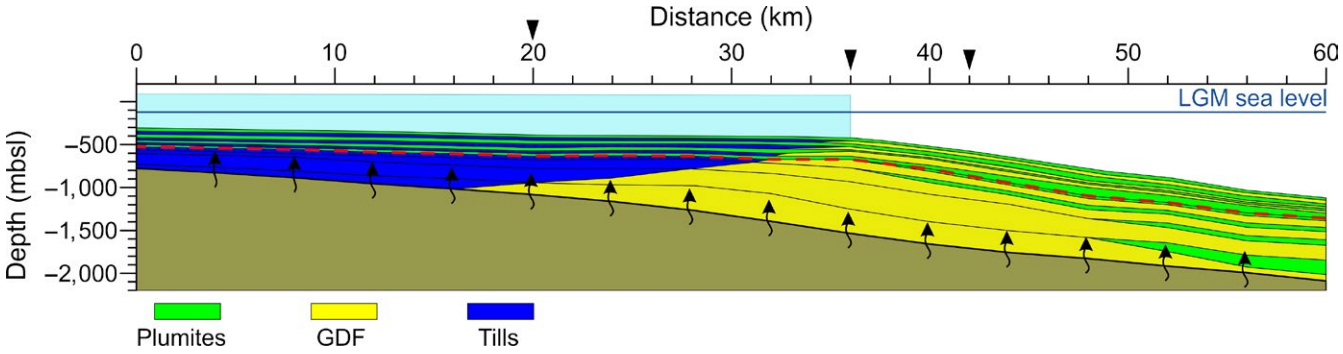

FIGURE 7 Conceptual margin stratigraphy and facies distribution used in the Plaxis model setup. During glacial maxima (GM) inter-glacial maximum (IGM) sediments are replaced by tills along the shelf to reproduce erosion of the underlying sediments and deposition of deformation tills during ice streams advance. Vertical exaggeration 4:1. Red dashed line depicts reflector R1. Black line with arrows depicts flow boundary condition at reflector R4A. Top inverted black triangles mark the location of synthetic wells. Light blue polygon shows ice configuration during the Last Glacial Maximum (LGM). Sea level corresponds to that of the LGM lowstand (Rohling et al., 2014)

From 19.5 ka to 13 ka, that is, during the last deglaciation phase, overpressure ratios decreased about 10% in the shallower 300 m. Only a few tens of metres right below the sea floor the model shows the same overpressure ratio values (ca. 0.4) than at the end of the LGM. At these shallow depths, overpressure ratios continued to decrease during the Holocene until values below 0.1 at present day (Figure 5d). Below 300 mbsf, overpressures remained between 0.2 and 0.4 along most of the margin.

Present-day excess pore pressures are lower than 12 MPa throughout most of the margin, and only the deepest areas in depocentres and the distal part of the margin show higher values that may attain up to 25 MPa (Figure 5a). At shallow depths (above ca. 300 mbsf), excess pore pressures are mostly below 5 MPa. However, near the main depocentre, close to the shelf edge, slightly higher excess pore pressures are present. In terms of present-day overpressures, the higher values in the shallower subsurface are expected in the outer shelf and lower slope with overpressure values below 0.4 according to the model (Figure 5).

4.2.2 | Detailed Late Quaternary hydrogeological evolution

The facies distribution along the Storfjorden TMF is well constrained from the seafloor to reflector R1 (see Llopart et al. (2015)) and such resolution is well suited for modelling with a finer FE mesh using PLAXIS. The sedimentation of the units involved in this setup starts at 1.2 Ma (age of horizon R4A). GDFs and tills extend over the shelf and upper slope up to horizon R1 (0.22 Ma). From that horizon to Present, the layer composition in the simulation is in agreement with the stratigraphy identified by Llopart et al. (2015). During Inter-Glacial Maximum (IGM) periods, the deposits consist almost entirely of plumites, while during Glacial Maxima (GM), plumites are replaced by tills along the shelf and GDFs are deposited along the slope. Replacement of plumites by tills along the shelf reproduces erosion of the underlying sediments and deposition of deformation tills during ice stream advance. In order to visualise the model evolution through time, parameters are logged at three positions: shelf (20 km), present-day shelf break (36 km) and upper slope (42 km; Figure 7). These points have been positioned to coincide with the first three wells in the BASIN model in order to be able to compare the results in both models. Because PLAXIS computes pore pressures after the first initial time step (1.2 to ca. 1.1 Ma), the modelled pressure evolution starts at 1.1 Ma.

To understand the role of undrained ice loading on fluid flow patterns, two sets of simulations were carried out as explained in the methods section. The fluid flow and pore pressure patterns as well as the resulting porosity and permeability fields are similar in both models but differ in magnitude. The model that accounts for ice loading develops higher overpressure ratios during the glacial maxima, when the shelf is loaded by ice. Overpressure ratios along the shelf may vary by as much as 0.4 in the shallow subsurface. Here, we concentrate the description in the model that accounts for ice loading and discuss the differences between the two models when tackling the effect of ice loading on margin hydrogeology later in the Discussion section.

Sediment physical properties (i.e. porosity and permeability) are clearly controlled by the consolidation due to

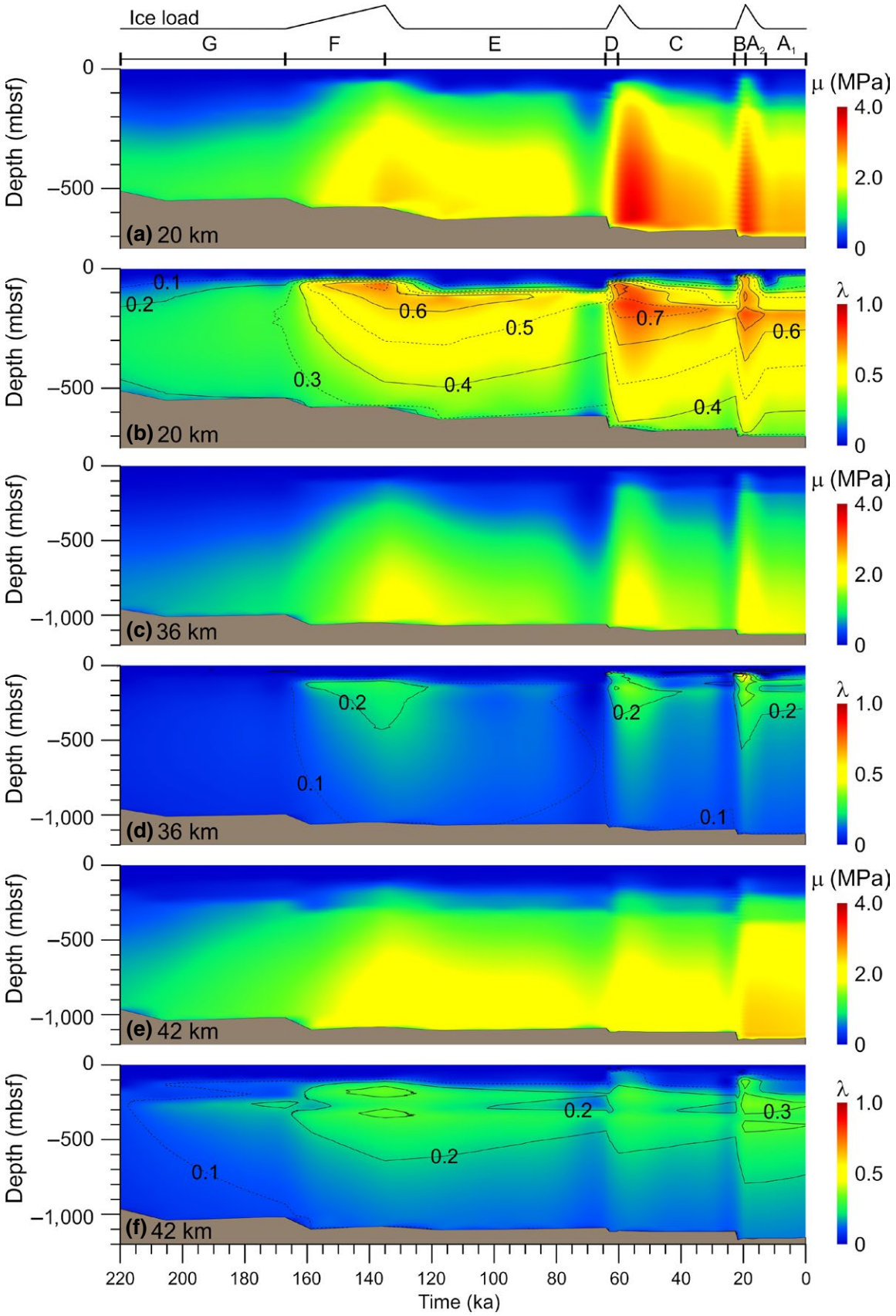

FIGURE 8 Time vs depth evolution of excess pore pressures (MPa) (a, c and e) and overpressure ratio (λ) (b, d and f) at the synthetic wells located at 20 (shelf), 36 (shelf edge) and 42 km (upper slope) along the model (see Figure 7 for location) for the model accounting for ice loading and unloading

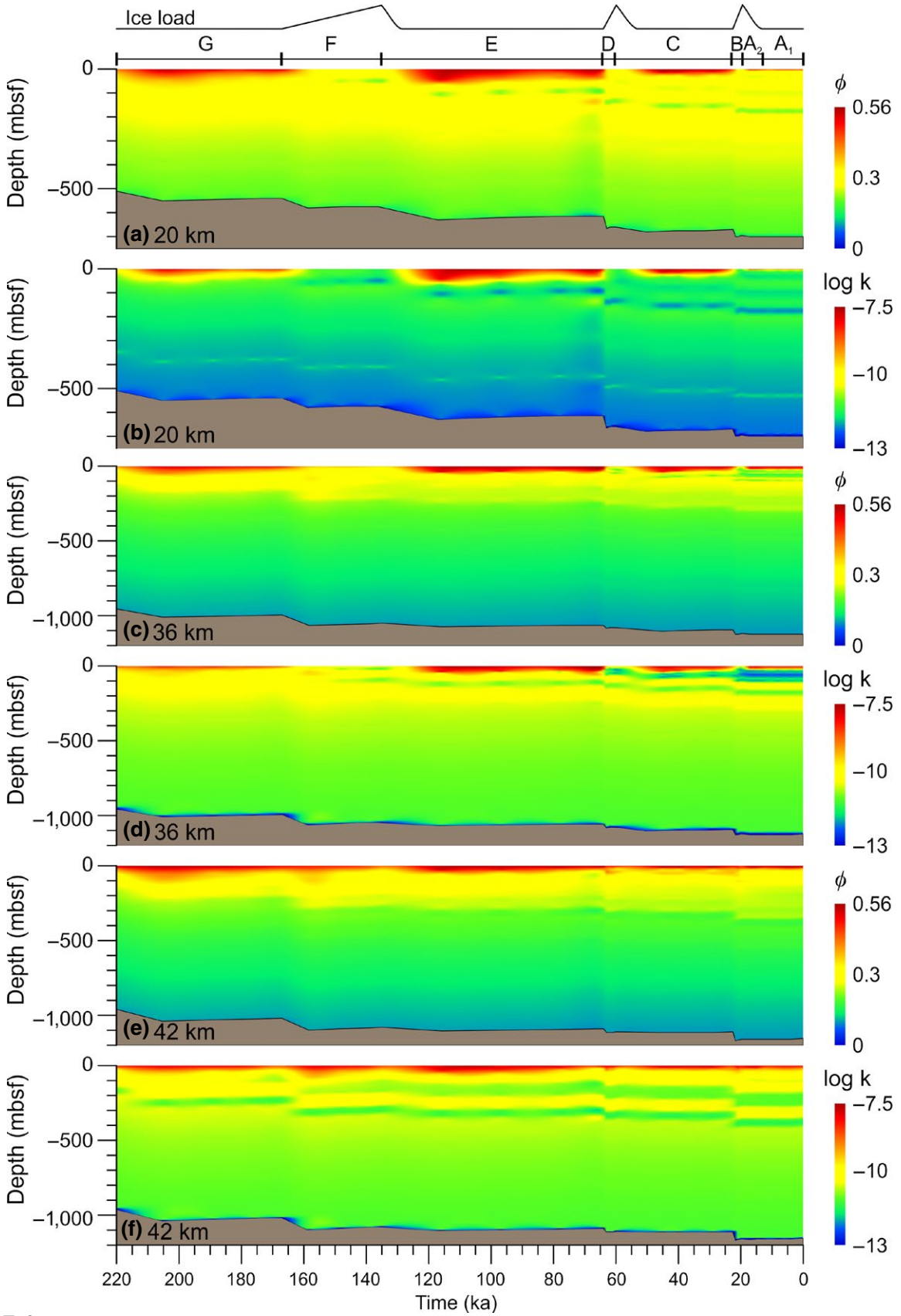

FIGURE 9 Time vs depth evolution of porosity (a, c and e) and hydraulic conductivity (m/s) (b, d and f) at the synthetic wells located at 20 (shelf), 36 (shelf edge) and 42 km (upper slope) along the model (see Figure 7 for location) for the model accounting for ice loading and unloading

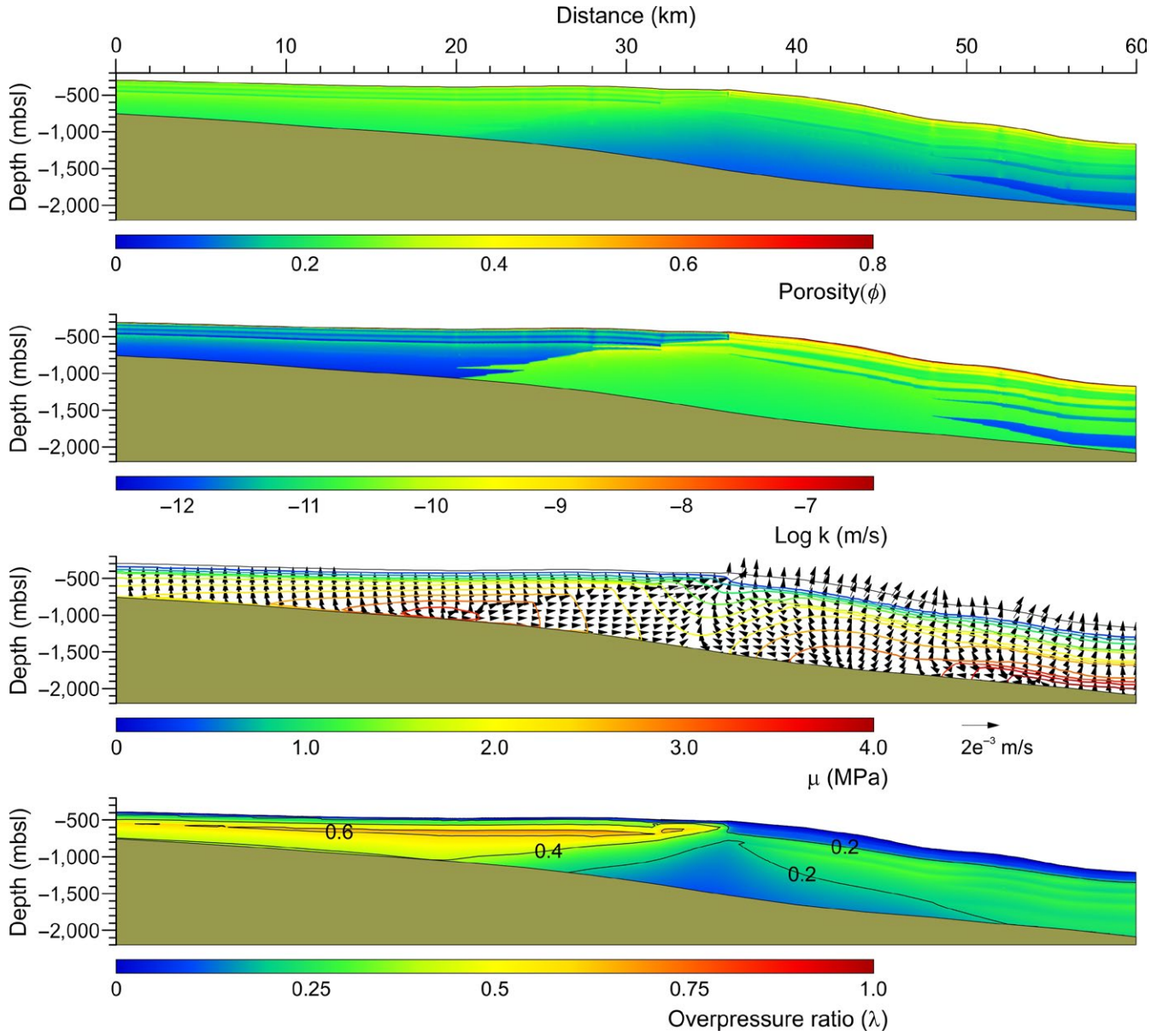

FIGURE 10 Margin stratigraphic and hydrodynamic modelling with Plaxis at final simulated Present day. (a) Fractional porosity, (b) Log hydraulic conductivity (m/s), (c) Excess pore pressure (MPa) and fluid flow (arrows; max 1.81e-11 m/s) and (d) Overpressure ratio (λ).Vertical exaggeration 4:1. Model accounting for ice loading

overburden. Therefore, from 1.2 to 0.22 Ma porosity and permeability decrease with depth with the lower values located at the shelf where tills are the prevailing sediment type. During sedimentation of unit U4A (1.2–0.99 Ma) pore pressures remain nearly hydrostatic. It is not until deposition of unit U4 (990 to 780 ka) that excess pore pressures (and overpressures) start to develop (see Supporting Information Figure S2). The highest excess pore pressures during deposition of sequence GII occur in deeper areas below the shelf with values up to 1 MPa (Supporting Information Figure S2a). Overpressure ratios during deposition of this sequence increased gradually in the slope area but values remained below 0.15 (Supporting Information Figure S2d,f). Deep below the shelf, however, overpressure ratios reached 0.35 (Supporting Information Figure S2b).

During deposition of sequence GIII (unit U1; 220 ka-Present), alternation between GM and IGM units is clearly reflected on the pore pressure evolution. Along the shelf, excess pore pressure increased in the entire sedimentary column even though values above 2.0 MPa occur only during the deposition of glacial units D and B (64–60 ka and 22.5–19.5 ka) (Figure 8a,c,e). At the shelf edge, the maximum excess pore pressure throughout the simulation (ca. 2.8 MPa) occurs below 450 mbsf during the LGM and remains relatively high till Present (Figure 8c). The increase in excess pore pressure during deposition of unit F (a GM unit) almost

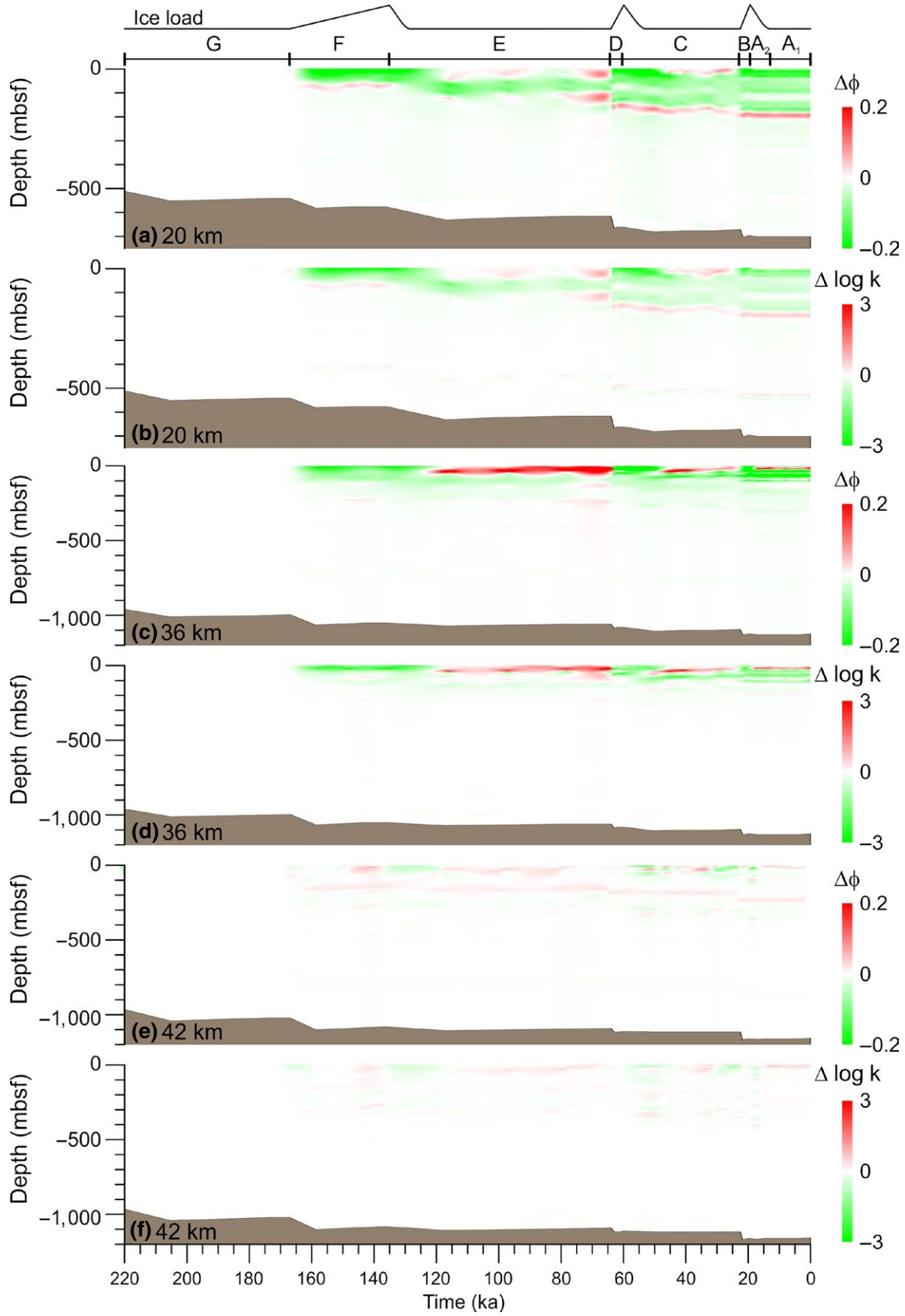

FIGURE 11 Comparison of the Plaxis output evolution between the models accounting/not accounting for ice load at the synthetic observation wells located at 20 (shelf), 36 (shelf edge) and 42 km (upper slope) along the model (see Figure 7 for location). Porosity (a, c and e) and log of hydraulic conductivity (m/s) (b, d and f). Shades of red in porosity/hydraulic conductivity imply higher values in the model accounting for ice loading

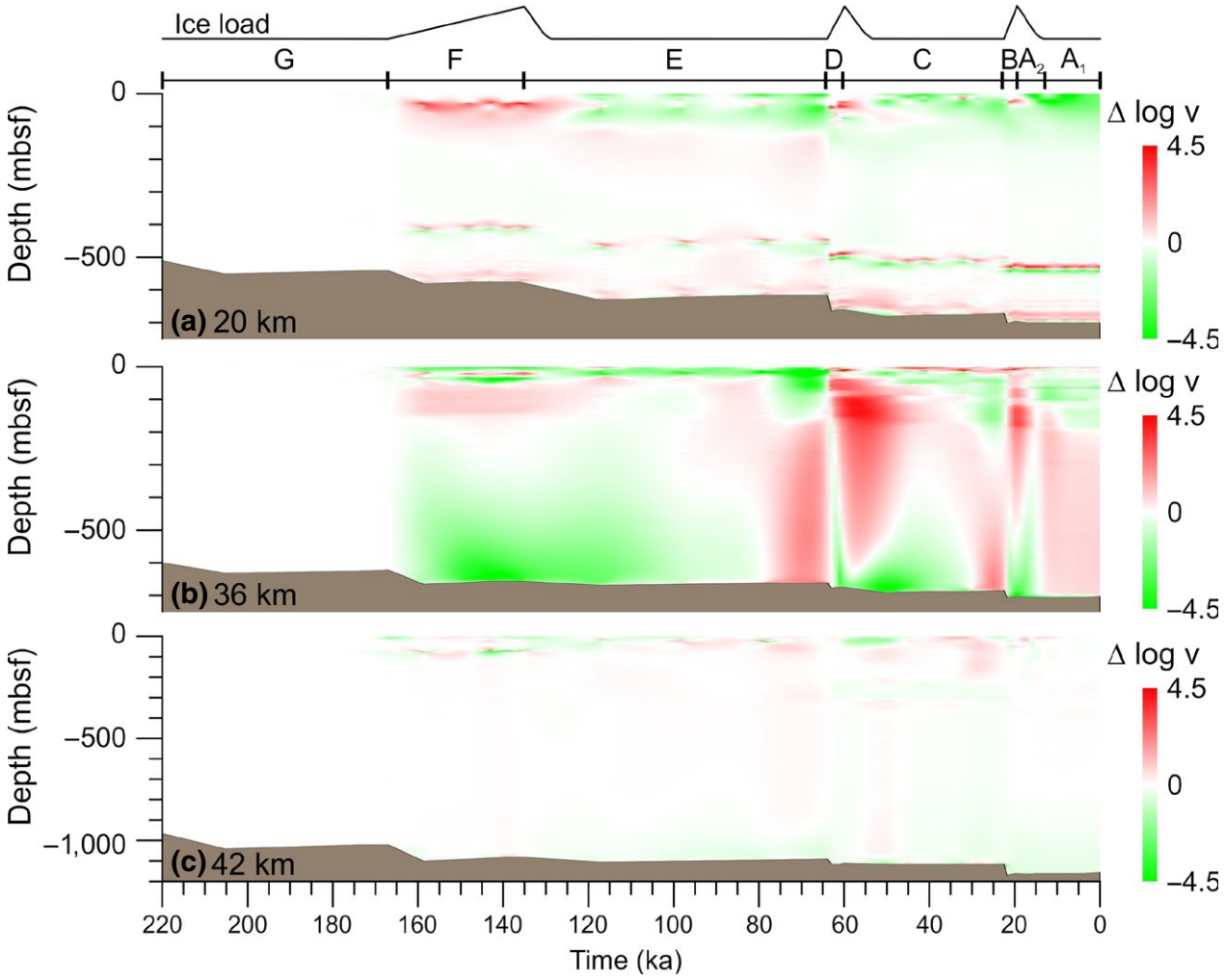

FIGURE 12 Comparison of the Plaxis output evolution in fluid flow rate (m/s) between the models accounting/not accounting for ice load at the synthetic observation wells located at 20 (shelf), 36 (shelf edge) and 42 km (upper slope) along the model (see Figure 7 for location). Velocity values coded in red mean higher fluid flow discharge in the model accounting for ice load. Simulated ice loading phases are shown on top with a black line

dissipated at the time of deposition of unit D (the second GM unit). Conversely, at the beginning of deposition of unit B, the LGM, excess pore pressures higher than 1.5–2 MPa had been preserved below 350 mbsf along the shelf and middle slope. In the entire model, excess pore pressures higher than 1 MPa are always located below 100–200 mbsf.

In terms of overpressure ratios, the highest values developed during deposition of sequence GIII in the first 200 m below the seabed and along the shelf with values ranging from 0.75 (close to lithostatic) during GM and 0.36 during IGM. Within these first 200 m below the shelf, the sedimentary intervals corresponding to IGM sediments are those displaying the highest overpressure during the last 60 kyrs (Figure 8b). Onset of overpressure development in the deepest of these intervals occurred during deposition of unit F (167 ka). High sedimentation rates during GM (up to 45 kg m^{-2} yr^{-1}), low initial permeability (10^{-12}–10^{-13} m/s) of the tills deposited over these plumites and the effect of undrained ice loading are responsible for such overpressure increase (Figures 7 and 8d). In particular, during deposition of unit D, between 64 and 60 ka, a significant overpressure increase occurred, which remained till the present day.

In the middle slope area, overpressure ratios higher than 0.35 occurred at depths above 70 mbsf during the LGM. Interestingly, the shelf edge area records lower overpressures at depth than the middle slope. While overpressures almost dissipated at the shelf edge and middle slope during the deglacial and interglacial periods, significant overpressures persisted along the shelf (Figure 8b,d,f). During the last deglacial and Holocene, the rate of dissipation of these overpressure ratios off the shelf was ca. 0.02 $kyrs^{-1}$, which correspond to excess pore pressures dissipation rates between 15 and 40 kPa/kyr (Figure 8c),

Contrasts in the porosity and permeability fields remain remarkably pronounced throughout the evolution of the margin (Figure 9). Porosity and permeability decrease with depth,

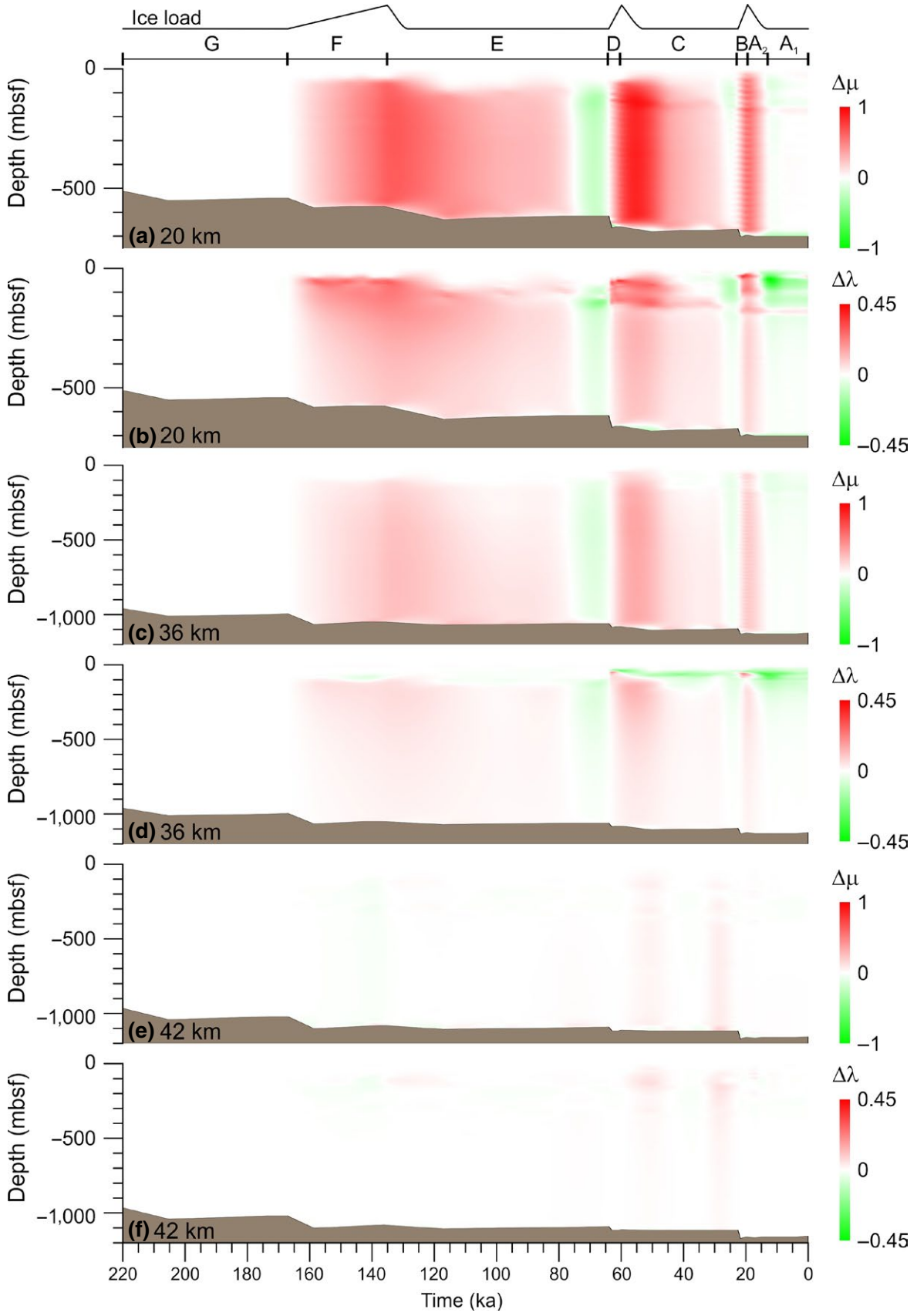

FIGURE 13 Comparison of the Plaxis output evolution between the models accounting/not accounting for ice load. Excess pore pressure (MPa) (a, c and e) and overpressure ratio (λ) (b, d and f) difference at the synthetic observation wells located at 20 (shelf), 36 (shelf edge) and 42 km (upper slope) (see Figure 7 for location). Shades of red in excess pore pressure/overpressure ratio imply higher values in the model accounting for ice loading

as it would be expected in a margin where porosity reduction is driven by normal compaction and consolidation. However, at shallow depths, layers of alternating high (plumites) and low (tills and GDFs) porosity and permeability are clearly depicted. The tills and GDFs at these shallow depths have hydraulic conductivity two orders of magnitude lower than the plumites immediately above and below them (Figure 9b,d,f). Deposition of GDFs causes initial overpressure, subsequent consolidation, discharge of the pore water in the plumites and partial dissipation of overpressure before deposition of a new set of GDFs during the next glaciation. However, at depths exceeding 1,000 mbsf, the porosity and hydraulic conductivity fields show that the units made of plumites are the ones that actually display lower porosity and hydraulic conductivity. Such low porosity and hydraulic conductivity results from the higher compressibility of these sediments compared to the surrounding GDFs (Figure 10a,b).

The modelled present-day overpressure ratios rapidly decrease off the shelf edge. In the upper slope, most overpressure values do not exceed 0.1, while the highest values of ca. 0.25 are limited to a single interval between 200 and 500 mbsf (Figure 10). On the other hand, overpressures in the middle slope are higher than those of the upper slope below 500 mbsf, but are rather similar for the upper 500 mbsf. In this area, overpressure ratio shows a slope parallel pattern of alternations between relatively low (0.2) and slightly higher values (0.3).

Along the margin, the fluid flow driven by the pore pressure field is mostly vertical, as expected for a continental margin where self-weight consolidation predominates. However, at some specific locations along the model the pattern differs from the usual upward flow (Figure 10c). The clearest example is the low-permeability till boundary on the shelf (and impervious ice), which diverts fluid flow towards the shelf edge acting as aquicludes. In a similar way, the low permeability of the plumite layers that develops when buried at depth makes those layers become middle slope aquitards and divert fluid towards the upper slope (Figure 10c). In this area, the fluid discharge is up to three orders of magnitude higher than in the shelf and two orders of magnitude higher than in the middle slope. However, high abundance of GDF deposits in the upper slope, which has little relative compressibility, allows for the preservation of permeability with depth and dissipation of excess pore pressures in the upper slope (Figure 10c).

5 | DISCUSSION

5.1 | Influence of glaciation on continental margin hydrogeology

In order to investigate the influence of ice loading on the margin during GM, two models were built with Plaxis (without and with ice load) and the results compared by subtracting one model from the other (ice model minus no-ice model; Figures 11–13). The undrained increase in total stress induced by the ice load leads to initial pore pressure build-up and slightly higher consolidation of the sediments below the shelf, with fluids escaping laterally to the upper slope. The porosity and permeability respond accordingly to such changes in total stress (Figure 11) and the sediments that were loaded by the ice acquired lower porosity and permeability than the sediments in the model where the ice loading is not considered. At the end of an IGM period, near-surface sediments (not loaded by ice) also display lower porosities and permeabilities in the model accounting for ice load than those in the model that does not account for ice load. These differences between the two models may be explained by contrasts in the rate of interstitial fluid discharge (Figure 12). When the shelf sediments are loaded by ice, the rate of interstitial fluid flow discharge to the seafloor at the shelf break is increased by ca. 10^{-4} m/s (Figure 12a). This vertical fluid flow discharge allows for further sediment consolidation, and hence a decrease in porosity and permeability (Figure 11).

The excess pore pressures that developed along the shelf sediments and in some areas of the middle slope are higher in the model that accounts for ice load not only during GM, but these higher excess pore pressures and overpressure ratios are preserved a significant amount of time during the following deglacial (Figure 13). The lower consolidation rate that occurred during glacials in the model that does not account for ice load, leads to lower porosity and permeability values ca. 18 kyrs after the end of a GM period. After these initial ca. 18 kyrs in the interglacial, and prior to the next GM, the model not accounting for ice load shows a higher rate of interstitial fluid discharge. The difference in fluid discharge between the two models is evident at the shelf edge (Figure 12), particularly at the end of interglacial period E (76 to 64 ka), whereas changes in porosity and permeability with burial history are more evident on the shelf, where ice loads have been applied (Figure 11). However, the influence of ice load in terms of porosity and permeability is also present on the upper slope and gradually decreases towards the middle slope. Differences in porosity and permeability between the two models vanish with depth and are almost nonexistent below 500 mbsf.

In general, the comparison (ice vs no-ice loading) at the three wells shows that the excess pore pressures and overpressure ratios are higher in the model where ice loading is considered (Figure 13). However, the maximum difference in excess pore pressure between the two models (up to 1 MPa) is not reached at the end of deposition of a GM unit, but during the following deglaciation. The same trend is present in the overpressure ratio field. The ice load induces an increase in overpressures of up to 0.45 in the shallower areas of the shelf, while at the shelf edge the difference between the two models is below 0.25

TABLE 4 Parameters derived from geotechnical tests in this study, mean values (μ), standard deviation (σ) and confidence interval (CI), for each physical property and sediment type, for a confidence level of 98%. Confident interval has been used to generate the input data for the Monte Carlo analysis. GDF: Glacigenic Debris Flows. ϕ_0: initial porosity at 1 kPa, k_0: decimal logarithm of initial hydraulic conductivity at ϕ_0, S_0: initial specific storage at ϕ_0

	SV02-02	SV02-03	SV02-04	SV03-04	SV02-05	SV02-06	GeoB17610-2-319	GeoB17610-2-330	No Sample
Sediment type	**Plumites**	**Plumites**	**Plumites**	**Plumites**	**GDF**	**GDF**	**Tills**	**Tills**	**Hemipelagics**
ϕ_0	0.60	0.65	0.63	0.65	0.50	0.48	0.48	0.48	–
μ	0.63				0.49		0.48		0.78
σ	0.025				0.014		0.002		0.025
CI	0.57–0.69				0.45–0.52		0.48–0.49		0.72–0.83
k_0 (*m/s*)	−8.64	−8.26	−8.14	−7.38	−9.44	−8.97	−9.31	−9.49	–
μ	−7.84				−9.14		−9.39		−8.52
σ	0.53				0.34		0.13		0.53
CI	−9.07 to −7.32				−9.93 to −8.36		−9.7 to −9.09		−9.75 to −7.29
S_0 (*m-1*)	0.024	0.019	0.032	0.026	0.009	0.007	0.006	0.004	–
μ	0.025				0.008		0.005		0.044
σ	0.005				0.001		0.001		0.005
CI	0.013–0.038				0.005–0.011		0.002–0.008		0.028–0.06

(Figure 13). This increase in overpressure ratio is related to the undrained ice loading on the shelf and higher fluid discharge rates on the shelf edge in the model accounting for ice load. The influence of ice loading in overpressure generation decreases towards the middle slope, where the difference between overpressure ratios in the two models is rather limited (ca. 0.1). However, the fact that a difference persists shows that the effect of ice loading on the continental shelf extends far beyond the shelf edge. The increase in overpressure difference between the two models is maximum at the end of the glaciations and persists during the following deglaciation: ca. 50 kyrs during deposition of unit E, ca. 10 kyrs during deposition of C and ca. 3 krys during the last deglaciation.

The differential model evolution shows that if the ice load is not taken into account during the glaciation, the fluid discharge is only controlled by the overburden induced by new sediment deposition. Therefore, only minor changes in loading rate occur that do not significantly modify consolidation trends in the passage from a glacial to a deglacial/interglacial stage. In fact, any change in consolidation trend is more subdued because of the higher fluid discharge from the less consolidated sediments below. This effect is clearly shown on the shelf, but not at the shelf edge (Figure 12b), because beyond this point no ice load is applied. The rate of ice loading (speed of ice advance and retreat) exerts a stronger control on the difference in porosity/permeability (and resulting overpressure) at the end of deposition of an IGM unit than the amount of ice load itself; the shorter the glaciation, the higher the fluid discharge and the shorter the time during which fluids are discharged at these high rates (Figures 11 and 12). In the middle slope, fluid discharge differences are lower than in the shelf, but the units primarily made of plumite sediments display higher fluid discharges in the model accounting for ice load (Figure 12). The higher permeability of plumites provides an efficient pathway for fluid evacuation towards the upper slope and excess pore pressure dissipation along the shelf. In turn, such increase in fluid discharge towards the plumites on the slope drives excess pore pressure (and overpressure) within these units on the slope because fluids cannot easily drain into the overlying lower permeability GDFs, thus hindering expulsion to the sea floor.

5.2 | Implications of hydrogeology for the slope stability on high-latitude continental margins

Along the Norwegian and western Barents Sea continental margin, a number of landslides of largely different sizes have been occurred (Haflidason, Lien, Sejrup, Forsberg, & Bryn, 2005; Laberg & Vorren, 2000; Sejrup et al., 2005). Most of these landslides are located at the side of nearby TMFs. The role of high sedimentation rates in the development of excess

pore pressure, weak layers and subsequent slope failure of high-latitude continental margins has already been highlighted (Urlaub, Talling, & Masson, 2013; Vanneste et al., 2012). However, here the modelled fluid flow only considers the interstitial water. No evidences of other fluid venting (i.e. gas mud or oil) or gas hydrates have been found in the Storfjorden and Kveithola TMFs. Nevertheless, fluid venting from deeper areas and dissociation and dissolution of gas hydrates are an additional factor that needs to be taken into account (Sultan, Cochonat, Foucher, & Mienert, 2004) in other places (i.e. western Barents Sea margin). Mulder and Moran (1995) also pointed that these high sedimentation rates coupled with static ice loading on the shelf during glacial maxima produce excess pore pressures that cannot be dissipated with the sediment and ice drainage capabilities. Such increase in excess pore pressures may lead to undrained failures in the upper slope and bearing capacity failures in the middle and lower slope (Mulder & Moran, 1995). The scarcity of age dating results prevents developing a statistical time frame for instabilities with respect to climate variability (Urlaub, 2013). However, stratigraphic data suggest that landslides occur indeed more frequently at certain periods, particularly during the deglaciation phase (Llopart et al., 2015). As shown in the previous sections, the highest overpressure ratios occurred related to the loading by ice streams during glacial maxima (Figure 8). The ice load has a significant effect on the development of overpressure ratio in shelf sediments that persists into the following deglacial and interglacial (Figure 13). It should be noted that the tills deposited during the glacial play also a significant role in the development of these overpressure and its preservation into the following deglacial period. Despite the undrained ice loading, interstitial flow to the shelf edge drives lower porosity and permeability (Figure 11), which impacts on the development of higher overpressures. However, these high overpressure ratios are limited to the shelf sediments where slope gradients are close to zero.

In the continental slope, where the gradients are steeper (2–3º) and most landslides occur, the effect of ice loading on the development of shallow overpressure ratios is a lot more subdued and is relatively significant only in the upper slope (Figure 13) where most shelf fluids are discharged (Figure 12). Here, loading by ice induces an increase in overpressure ratio up to ca. 0.5, almost doubling the amount of overpressure (ca. 0.2 higher compared to the model that only accounts for sediment loading). In the middle slope, ice loading on the shelf has minimal influence (Figure 13e,f). Nevertheless, excess pore pressure also builds up (Figure 8e). The origin of such excess pore pressure should be sought in the depositional pattern: alternating glacial and glaciomarine sedimentary conditions produce deposition of materials with contrasting mechanical and hydraulic properties although these differences decrease with burial (Figures 9 and 10). In this regard, it is clear that deglacial plumites played a significant role in the onset of slope failure, since overpressure mainly develops within these porous and more permeable deposits (Figures 8 and 10).

The results from the models indicate that the sedimentary architecture developed throughout TMF progradation during glacial stages led to the development of focused fluid flow towards the uppermost slope and allowed modest to high overpressures to be maintained during the first 1,000 years during the following deglaciation. It is indeed during deglaciations when most of the landslides identified in the Storfjorden and Kveithola TMFs seem to have occurred (Llopart et al., 2015; Lucchi et al., 2012). Since the factors driving overpressure in our models are common to all high-latitude continental margins, a similar pattern of overpressure build-up during glaciations and cyclic landslide occurrence might exist in all sedimentary wedges of these margins. The models show that glacigenic sedimentation induces a marked cyclicity in pore pressure and overpressure trends and that loading by ice on the

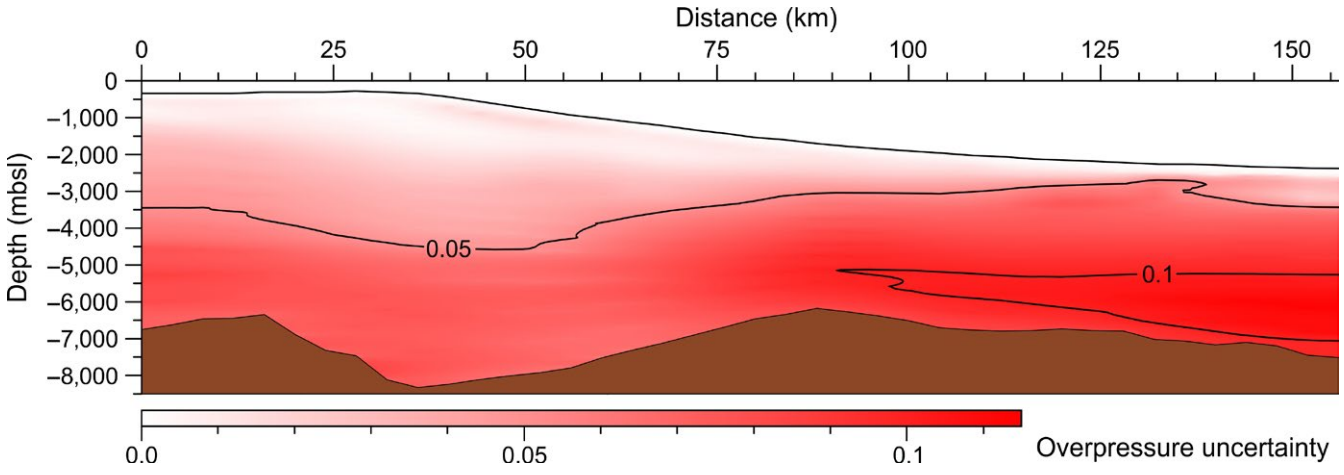

FIGURE 14 Uncertainty in overpressure results derived from variability in mechanical and hydraulic properties using a Monte Carlo analysis over BASIN

shelf only intensifies the differences between glacial maxima and interglacials. The model that takes into account the ice loading shows that the permeable sediments of previous deglacials display higher overpressure ratios during the early deglacial. However, they also show that overpressure within these sediments subsequently dissipates likely producing more stable conditions during the late deglacial and interglacial than those in the model that does not account for ice loading. Therefore, this study indicates that ice loading contributes to a more marked cyclicity and clustering of landslides at specific times within the glacial cycle. However, whether the moderate overpressures on the upper and middle slope, modelled for the early deglaciation, were high enough to trigger the observed failures and what other mechanisms could have played a role in the onset of slope failure, will need further investigation.

A first aspect to consider is that local sediment variations with respect to the models presented in this study cannot be excluded. The existence of more permeable sediments such as water-rich contourite layers within the IGM units, could lead to further overpressure development within these units (Baeten et al., 2014). Contourites are also more sensitive and have a more brittle nature than plumites, that could favour the formation of glide planes (Bryn, Berg, Stoker, Haflidason, & Solheim, 2005).

Most importantly, it has been pointed out that the loading applied by earthquakes during the deglaciation due to the isostatic rebound could lead to slope failures (Bellwald, Hjelstuen, Sejrup, & Haflidason, 2016; L'Heureux et al., 2013). Hampel, Hetzel, Maniatis, and Karow (2009) modelled the seismicity associated to fault reactivation during ice advance and retreat obtaining plausible earthquake scenarios of magnitude $M_w \approx 8$. Hampel et al. (2009) further stressed out that most seismicity from isostatic rebound is associated with the deglaciation phase. In addition, Bungum, Lindholm, and Faleide (2005) suggested that earthquakes of magnitude $M_w \approx 6.5$–7 could occur up to 5–6 kyrs after the last deglaciation. The Hornsund Fault Zone crosses the outer shelf of the Storfjorden and Kveithola troughs and could lead to significant earthquakes. The ground motions generated by those earthquakes on the Storfjorden TMF could easily induce the slope failures observed in the area. Further investigations may consider the coupling of the isostatic rebound triggered earthquakes with a slope already pre-conditioned for failure with relatively high overpressure.

5.3 | Uncertainty in models results

As for all type of modelling, the exercises performed in the previous section are prone to potential sources of output uncertainty. These derive from parameter and transformation uncertainties(Nadim, 2015). Transformation uncertainties are due to the approximations and simplifications inherent to the models. Parameter uncertainties are related to the models structure and variability in mechanical and hydraulic properties. The first incorporates seismic data resolution issues, choice of relationship for time to depth conversion, accuracy of sound speed determination and uncertainties in facies attribution (together with heterogeneity) along the modelled transect. Basin analysis models are commonly developed by utilising the best available information to construct one deterministic geological model and the uncertainties resulting from the model structure are thus hard to evaluate. Potential ways to estimate these uncertainties are reviewed in Nilsson, Højberg, Refsgaard, and Troldborg (2007) and are beyond the scope of the present study. With regard to the variability in mechanical and hydraulic properties, Monte Carlo analysis provides a way to assess their influence on output uncertainty (in this case pore pressure and overpressure). We use BASIN (Bitzer, 1999) as the numerical model for the analysis because of the lower computational demand.

When models are made of independent variables, the ideal approach would be to test the influence of the different geotechnical parameters used in the simulation one at a time. In this case, such approach is, however, not adequate because porosity, permeability and compressibility/specific storage are interdependent parameters. A decrease in the porosity has to be associated also to a decrease in the other two parameters, and vice versa. Thus, when porosity is increased, permeability and specific storage need to be increased as well following the regression curves obtained from the geotechnical tests. A set of confidence intervals (CI) (instead of the standard deviation given the reduced number of geotechnical tests) for each sediment type and geotechnical property (Table 4) is the input for the Monte Carlo analysis. Due to lack of tests on hemipelagic sediments, the confidence intervals from plumites have been used for this sediment type. The set of initial parameters created for Monte Carlo analysis with BASIN has been obtained by using a Simple Random Sampling (SRS) in between the range of the confidence interval with a confidence level of 98% (Hurtado & Barbat, 1998). Hence, a total of 512 models have been computed by creating the parameter sets randomly. The results of overpressure from all the models have been averaged and the standard deviation to the reference model (Figure 5) has been calculated (Figure 14).

Given the available mechanical and hydraulic data, the output from the Monte Carlo simulation shows that the mean value of uncertainty in the whole model is around 5%-7%. The maximum uncertainty, around 12%, occurs chiefly in the area where hemipelagic sediments are thicker (distal part). However, the analysis shows that plumites have a significant contribution to uncertainty. The low variability in the GDFs and tills physical properties is reflected in a lower uncertainty

where they are the predominant sediment type. A larger number of geotechnical tests on these sediments could ascertain whether this uncertainty is genuine.

6 | CONCLUSIONS

Compressibility and permeability testing of glacial and glacially influenced sediments of the Storfjorden outer shelf and upper slope show that plumites (deglacial meltwater sediments) have higher void ratios and permeabilities with respect to GDFs and tills at initial deposition conditions. Also, the compressibility index of plumites is higher than that of GDFs and tills. The tested till sediments show low over-consolidation ratios (OCRca. 1.5), which are interpreted to be a result of undrained ice loading conditions.

A long-term model evolution of the Storfjorden TMF from 2.7 to Present shows that the onset of glacial sedimentation (ca. 1.5 Ma) had a significant role in developing aquicludes (tills) on the shelf, which led to a decrease in vertical fluid flow and diversion of this flow towards the slope. The occurrence of these aquicludes with concomitant aquitards (plumites) on the continental slope significantly influenced the fluid migration pathways on the continental margin. Prior to 220 ka the highest overpressure ratios in shallow sediments (few 100 m below seafloor) had developed in the shelf. However, higher values are depicted in the lower slope (λ ca. 0.5) where highly compressible and water-rich fine sediments are present.

In order to investigate the role of ice loading during glacial maxima on the overpressure build-up, two higher resolution models (accounting for ice load or not) spanning the last 1.2 Ma have been elaborated. These models are focused on the last 220 kyr. The differences between the two models show that undrained ice loading has a major impact on the development of overpressures in shelf and shelf edge sediments (up to λ ca. 0.75 during glacial maxima and up to 0.36 at the end of an interglacial). Undrained ice loading and/or deposition of low-permeability tills on the shelf, induces flow focusing towards the most permeable sediments in the upper slope (plumites) increasing their overpressure. On the slope, loading of plumite sediments by GDFs is the main factor driving overpressure, which may attain values up to 0.5. The less permeable GDFs hinder fluid evacuation from plumite layers towards the sea floor. Shelf loading by ice and tills, and associated diversion of fluids to the upper-middle slope, have a relatively minor contribution to overpressure development on slope sediments with only a 10% increase in overpressure when ice loading of the shelf sediments is considered. The models highlight that overpressure ratios along the slope have dropped at the end of an interglacial by 50% compared to previous Glacial Maxima. However, relatively high overpressure ratios remain during the early deglaciation phase.

The overpressure developed within the plumite layers clearly decreases their shear strength and bearing capacity. Plumite layers therefore become weakened layers and are a first-order pre-conditioning factor for slope failures. Hence, the current study significantly enhances the knowledge on the mechanisms that drive the overpressure and the timing of landslides within a glacial cycle in high-latitude continental margins. Nevertheless, the values of overpressure ratio within these plumites (up to 0.5) and the timing of landslides during early deglaciation call for an added minor external trigger. Earthquakes from post-glacial isostatic rebound are the most likely candidate.

ACKNOWLEDGEMENTS

This study is funded by the 'Ministerio Economia y Competitividad' through grants DEGLABAR, (CTM2010-17386), CORIBAR-ES (CTM2011-14807-E) and SVAIS (POL2006-07390). UNESCO and IUGS are also acknowledged for funding through projects IGCP-585 and IGCP-640. The Italian contribution was supported by PNRA project 2013/B2.08 VALFLU. Plaxis is acknowledged for a Plaxis 2D educational license. The data reported in this paper are archived in Pangaea (www.pangaea.de).

ORCID

Jaume Llopart https://orcid.org/0000-0002-9495-1194

REFERENCES

Baeten, N. J., Laberg, J. S., Vanneste, M., Forsberg, C. F., Kvalstad, T. J., Forwick, M., … Haflidason, H. (2014). Origin of shallow submarine mass movements and their glide planes-Sedimentological and geotechnical analyses from the continental slope off northern Norway. *Journal of Geophysical Research: Earth Surface*, *119*(11), 2335–2360. https://doi.org/10.1002/2013JF003068

Bellwald, B., Hjelstuen, B. O., Sejrup, H. P., & Haflidason, H. (2016). 'Postglacial mass movements and depositional environments in a high-latitude fjord system – Hardangerfjorden, Western Norway. *Marine Geology*, *379*, 157–175. https://doi.org/10.1016/j.margeo.2016.06.002

Bitzer, K. (1996). Modeling consolidation sedimentary and fluid basins flow. *Computers & Geosciences*, *22*(5), 467–478. https://doi.org/10.1016/0098-3004(95)00113-1

Bitzer, K. (1999). Two-dimensional simulation of clastic and carbonate sedimentation, consolidation, subsidence, fluid flow, heat flow and solute transport during the formation of sedimentary basins. *Computers & Geosciences*, *25*(4), 431–447. https://doi.org/10.1016/S0098-3004(98)00147-2

Boudreau, B. P. (1996). The diffusive tortuosity of fine-grained unlithified sediments. *Geochimica et Cosmochimica Acta*, *60*(16), 3139–3142. https://doi.org/10.1016/0016-7037(96)00158-5

British Standards Institution (1990) Part 6. Consolidation and permeability test in hydraulic cells and with pore pressure measurement.

In: Soils for civil engineering purposes. Road Enineering Satndards Committee, p. 61.

Bryn, P., Berg, K., Stoker, M., Haflidason, H., & Solheim, A. (2005). Contourites and their relevance for mass wasting along the Mid-Norwegian Margin. *Marine and Petroleum Geology*, *22*(1–2), 85–96. https://doi.org/10.1016/j.marpetgeo.2004.10.012

Bungum, H., Lindholm, C., & Faleide, J. I. (2005). Postglacial seismicity offshore mid-Norway with emphasis on spatio-temporal-magnitudal variations. *Marine and Petroleum Geology*, *22*(1–2), 137–148. https://doi.org/10.1016/j.marpetgeo.2004.10.007

Butt, F. A., Elverhøi, A., Solheim, A., & Forsberg, C. F. (2000). Deciphering late cenozoic development of the western Svalbard Margin from ODP Site 986 results. *Marine Geology*, *169*(3–4), 373–390. https://doi.org/10.1016/S0025-3227(00)00088-8

Christoffersen, P., & Tulaczyk, S. (2003). Signature of palaeo-ice-stream stagnation: Till consolidation induced by basal freeze-on. *Boreas*, *32*(1), 114–129. https://doi.org/10.1111/j.1502-3885.2003.tb01433.x

Dahlgren, K. I., Vorren, T. O., Stoker, M. S., Nielsen, T., Nygård, A., & Petter Sejrup, H. (2005). Late Cenozoic prograding wedges on the NW European continental margin: Their formation and relationship to tectonics and climate. *Marine and Petroleum Geology*, *22*(9–10), 1089–1110. https://doi.org/10.1016/j.marpetgeo.2004.12.008

Dowdeswell, J. A., Elverhøi, A., & Spielhagen, R. (1998). Glacimarine sedimentary processes and facies on the Polar North Atlantic margins. *Quaternary Science Reviews*, *17*(1–3), 243–272. https://doi.org/10.1016/S0277-3791(97)00071-1

Dowdeswell, J. A., & Siegert, M. J. (1999). Ice-sheet numerical modeling and marine geophysical measurements of glacier-derived sedimentation on the Eurasian Arctic continental margins. *Geological Society of America Bulletin*, *111*(7), 1080–1097. https://doi.org/10.1130/0016-7606(1999) 111<1080:ISNMAM>2.3.CO;2

Dugan, B., & Sheahan, T. C. (2012). Offshore sediment overpressures of passive margins: Mechanisms, measurement, and models. *Reviews of Geophysics*, *50*(3), 1–20. https://doi.org/10.1029/2011RG000379

Eldholm, O., Sundvor, E., Myhre, A. M., & Faleide, J. I. (1984) Cenozoic evolution of the continental margin off Norway and western Svalbard. In A. M. Spencer (Ed.), *Petroleum Geology of the North European Margin* (pp. 3–18). Dordrecht, the Netherlands: Springer. https://doi.org/10.1007/978-94-009-5626-1

Engelhardt, H., & Kamb, B. (1997). Basal hydraulic system of a West Antarctic ice stream: Constraints from borehole observations. *Journal of Glaciology*, *43*(144), 207–230. https://doi.org/10.3189/S0022143000003166

Faleide, J. I., Solheim, A., Fiedler, A., Hjelstuen, B. O., Andersen, E. S., & Vanneste, K. (1996). Late Cenozoic evolution of the western Barents Sea-Svalbard continental margin. *Global and Planetary Change*, *12*(1–4), 53–74. https://doi.org/10.1016/0921-8181(95)00012-7

Faleide, J. I., Vdgnes, E., & Gudlaugsson, S. T. (1993). Late Mesozoic-Cenozoic evolution of the south-western Barents Sea in a regional rift-shear tectonic setting. *Marine and Petroleum Geology*, *10*, 186–214. https://doi.org/10.1016/0264-8172(93)90104-Z

Fiedler, A., & Faleide, J. I. (1996). Cenozoic sedimentation along the southwestern Barents Sea margin in relation to uplift and erosion of the shelf. *Global and Planetary Change*, *12*(1–4), 75–93. https://doi.org/10.1016/0921-8181(95)00013-5

Flemings, P., Long, H., Dugan, B., Germaine, J., John, C., Behrmann, J., & Sawyer, D. (2008). Pore pressure penetrometers document high overpressure near the seafloor where multiple submarine landslides have occurred on the continental slope, offshore Louisiana, Gulf of Mexico. *Earth and Planetary Science Letters*, *269*(3–4), 309–325. https://doi.org/10.1016/j.epsl.2007.12.005

Forsberg, C. F., Solheim, A., Jansen, E., & Andersen, E. S. (1999). The depositional enviroment of the western svalbard margin during the late pliocene and the pleistocene: Sedimentary facies changes at site 986. *Proceedings of the Ocean Drilling Program, Scientific Results*, *162*, 233–246. https://doi.org/10.2973/odp.proc.sr.162.1999

Gutierrez, M., & Wangen, M. (2005). Modeling of compaction and overpressuring in sedimentary basins. *Marine and Petroleum Geology*, *22*(3), 351–363. https://doi.org/10.1016/j.marpetgeo.2005.01.003

Haflidason, H., Lien, R., Sejrup, H. P., Forsberg, C. F., & Bryn, P. (2005). The dating and morphometry of the Storegga Slide. *Marine and Petroleum Geology*, *22*(1–2), 123–136. https://doi.org/10.1016/j.marpetgeo.2004.10.008

Hampel, A., Hetzel, R., Maniatis, G., & Karow, T. (2009). Three-dimensional numerical modeling of slip rate variations on normal and thrust fault arrays during ice cap growth and melting. *Journal of Geophysical Research*, *114*(B8), B08406. https://doi.org/10.1029/2008JB006113

Hesse, R., Khodabakhsh, S., Klaucke, I., & Ryan, W. B. F. (1997). Asymmetrical turbid surface-plume deposition near ice-outlets of the Pleistocene Laurentide ice sheet in the Labrador Sea. *Geo-Marine Letters*, *17*(3), 179–187. https://doi.org/10.1007/s003670050024

Hjelstuen, B. O., Elverhøi, A., & Faleide, J. I. (1996). Cenozoic erosion and sediment yield in the drainage area of the Storfjorden Fan. *Global and Planetary Change*, *12*(1–4), 95–117. https://doi.org/10.1016/0921-8181(95)00014-3

Hurtado, J. E., & Barbat, A. H. (1998). Monte carlo techniques in computational stochastic mechanics. *Archives of Computational Methods in Engineering*, *5*(1), 3–29. https://doi.org/10.1007/BF02736747

Jansen, E., Raymo, M. E., Blum, P., & Al, E. (1996). *Site 986, Proceedings of the Ocean Drilling Program, 162 Initial Reports*. College Station, TX: Ocean Drilling Program. https://doi.org/10.2973/odp.proc.ir.162.109.1996

Javanshir, R. J., Riley, G. W., Duppenbecker, S. J., & Abdullayev, N. (2015). 'Validation of lateral fluid flow in an overpressured sand-shale sequence during development of Azeri-Chirag-Gunashli oil field and Shah Deniz gas field: South Caspian Basin, Azerbaijan. *Marine and Petroleum Geology*, *59*, 593–610. https://doi.org/10.1016/j.marpetgeo.2014.07.019

Knies, J., Matthiessen, J., Vogt, C., Laberg, J. S., Hjelstuen, B. O., Smelror, M., … Vorren, T. O. (2009). The Plio-Pleistocene glaciation of the Barents Sea-Svalbard region: A new model based on revised chronostratigraphy. *Quaternary Science Reviews*, *28*(9–10), 812–829. https://doi.org/10.1016/j.quascirev.2008.12.002

Kvalstad, T. J., Andresen, L., Forsberg, C. F., Berg, K., Bryn, P., & Wangen, M. (2005). The Storegga slide: Evaluation of triggering sources and slide mechanics. *Marine and Petroleum Geology*, *22*(1–2), 245–256. https://doi.org/10.1016/j.marpetgeo.2004.10.019

Kyrke-Smith, T. M., Katz, R. F., & Fowler, A. C. (2013). Subglacial hydrology and the formation of ice streams. *Proceedings of the Royal Society A: Mathematical, Physical and Engineering Sciences*, *470*(2161), 20130494. https://doi.org/10.1098/rspa.2013.0494

Laberg, J. S., Andreassen, K., Knies, J., Vorren, T. O., & Winsborrow, M. (2010). Late pliocene-pleistocene development of the barents sea ice sheet. *Geology*, *38*(2), 107–110. https://doi.org/10.1130/G30193.1

Laberg, J. S., Forwick, M., & Husum, K. (1996). Proceedings of the Ocean Drilling Program, 162 Initial Reports. In E. Jansen et al. (Ed.), *Ocean Drilling Program (Proceedings of the Ocean Drilling Program)*, 162(ii), p. 2973. https://doi.org/10.2973/odp.proc.ir.162.1996

Laberg, J. S., & Vorren, T. O. (1996). The glacier-fed fan at the mouth of Storfjorden trough, western Barents Sea: A comparative study. *Geologische Rundschau*, *00*, 338–349. https://doi.org/10.1007/bf02422239

Laberg, J. S., & Vorren, T. O. (2000). The Trænadjupet Slide, offshore Norway - Morphology, evacuation and triggering mechanisms. *Marine Geology*, *171*(1–4), 95–114. https://doi.org/10.1016/S0025-3227(00)00112-2

Landvik, J. Y., Bondevik, S., Elverhøi, A., Fjeldskaar, W., Mangerud, J., Salvigsen, O., … Vorren, T. O. (1998). Last glacial maximum of svalbard and the barents sea area: Ice sheet extent and configuration. *Quaternary Science Reviews*, *17*(1–3), 43–75. https://doi.org/10.1016/S0277-3791(97)00066-8

Leynaud, D., Sultan, N., & Mienert, J. (2007). The role of sedimentation rate and permeability in the slope stability of the formerly glaciated Norwegian continental margin: The Storegga slide model. *Landslides*, *4*(4), 297–309. https://doi.org/10.1007/s10346-007-0086-z

L'Heureux, J. S., Vanneste, M., Rise, L., Brendryen, J., Forsberg, C. F., Nadim, F., … Haflidason, H. (2013). 'Stability, mobility and failure mechanism for landslides at the upper continental slope off Vesterålen, Norway. *Marine Geology*, *346*, 192–207. https://doi.org/10.1016/j.margeo.2013.09.009

Llopart, J., Urgeles, R., Camerlenghi, A., Lucchi, R. G., De Mol, B., Rebesco, M., & Pedrosa, M. T. (2014) Slope Instability of Glaciated Continental Margins: Constraints from Permeability-Compressibility Tests and Hydrogeological Modeling Off Storfjorden, NW Barents Sea. In S. Krastel et al. (Ed.), *Submarine Mass Movements and Their Consequences, Advances in Natural and Technological Hazards Research 37* (pp. 95–104). Switzerland: Springer International Publishing. https://doi.org/10.1007/978-3-319-00972-8_9

Llopart, J., Urgeles, R., Camerlenghi, A., Lucchi, R. G., Rebesco, M., & De Mol, B. (2015). Late Quaternary development of the Storfjorden and Kveithola Trough Mouth Fans, northwestern Barents Sea. *Quaternary Science Reviews*, *129*, 68–84. https://doi.org/10.1016/j.quascirev.2015.10.002

Lucchi, R. G., Camerlenghi, A., Colmenero-hidalgo, E., Sierro, F. J., Bárcena, A., Flores, J., … Sagnotti, L. (2010) Sedimentary processes on the Storfjorden trough-mouth fan during last deglaciation phase : The role of subglacial meltwater plumes on continental margin sedimentation. In *Geophycal Research Abstracts*. Oral Presentation, EGU General Assembly, 2010, May 3–7 2010, Vienna (Austria). Geophysical Research Abstracts, Vol. 12, EGU2010-5753-2., p. 1.

Lucchi, R. G., Camerlenghi, A., Rebesco, M., Colmenero-Hidalgo, E., Sierro, F. J., Sagnotti, L., … Caburlotto, A. (2013). Postglacial sedimentary processes on the Storfjorden and Kveithola trough mouth fans: Significance of extreme glacimarine sedimentation. *Global and Planetary Change*, *111*, 309–326. Elsevier B.V. https://doi.org/10.1016/j.gloplacha.2013.10.008

Lucchi, R. G., Pedrosa, M. T., Camerlenghi, A., Urgeles, R., De Mol, B., & Rebesco, M. (2012) Recent Submarine Landslides on the Continental Slope of Storfjorden and Kveithola Trough-Mouth Fans (North West Barents Sea). In Y. Yamada, et al. (Eds.), *Submarine Mass Movements and Their Consequences, Advances in Natural and Technological Hazards Research 31* (pp. 735–745). Dordrecht, the Netherlands: Springer. https://doi.org/10.1007/978-94-007-2162-3

Marín-Moreno, H., Minshull, T. A., & Edwards, R. A. (2013). A disequilibrium compaction model constrained by seismic data and application to overpressure generation in The Eastern Black Sea Basin. *Basin Research*, *25*, 331–347. https://doi.org/10.1111/bre.12001

Mulder, T., & Moran, K. (1995). Relationship among submarine instabilities, sea level variations, and the presence of an ice sheet on the continental shelf: An example from the Verrill Canyon Area, Scotia Shelf. *Paleoceanography*, *10*(1), 137–154. https://doi.org/10.1029/94PA02352

Nadim, F. (2015). Accounting for Uncertainty and Variability in Geotechnical Characterization of Offshore Sites. In T. Schweckendiek et al. (Eds.), *Geotechnical Safety and Risk V*, Amsterdam, Netherlands: IOS Press.

Nilsson, B., Højberg, A. L., Refsgaard, J. C., & Troldborg, L. (2007). Uncertainty in geological and hydrogeological data. *Hydrology and Earth System Sciences*, *11*(5), 1551–1561. https://doi.org/10.5194/hess-11-1551-2007

Ó Cofaigh, C., Andrews, J. T., Jennings, A. E., Dowdeswell, J. A., Hogan, K. A., Kilfeather, A. A., & Sheldon, C. (2013). Glacimarine lithofacies, provenance and depositional processes on a West Greenland trough-mouth fan. *Journal of Quaternary Science*, *28*(1), 13–26. https://doi.org/10.1002/jqs.2569

Ó Cofaigh, C., Taylor, J., Dowdeswell, J. A., & Pudsey, C. J. (2003). Palaeo-ice streams, trough mouth fans and high-latitude continental slope sedimentation. *Boreas*, *32*, 37–55. https://doi.org/10.1080/03009480310001858

Ó Cofaigh, C., Taylor, J., Dowdeswell, J. A., Rosell-Melé, A., Kenyon, N. H., Evans, J., & Mienert, J. (2002). Sediment reworking on high-latitude continental margins and its implications for palaeoceanographic studies: insights from the Norwegian-Greenland Sea. *Geological Society, London, Special Publications*, *203*(1), 325–348. https://doi.org/10.1144/gsl.sp.2002.203.01.17

Pedrosa, M. T., Camerlenghi, A., De Mol, B., Urgeles, R., Rebesco, M., & Lucchi, R. G. (2011). Seabed morphology and shallow sedimentary structure of the Storfjorden and Kveithola trough-mouth fans (North West Barents Sea). *Marine Geology*, *286*(1–4), 65–81. https://doi.org/10.1016/j.margeo.2011.05.009

PLAXIS bv (2015) *Plaxis 2015 User's Manual*. Delf, The Netherlands: PLAXIS bv.

Raymo, M. E., E. Jansen, P. Blum, & T. D. Herbert (Eds.) (1999). *Proceedings of the Ocean Drilling Program, 162 Scientific Results (Vol. 162)*. College Station, TX: Ocean Drilling Program.

Raymo, M. E., Jansen, E., Blum, P., & Herbert, T. D. (Eds.), (2002). Proceedings of the Ocean Drilling Program, Scientific Results. In *Data report: Radiolarians in sediments from the Palmer Deep, Antarctica, Leg 178, Site 1098* (Vol. *178*, Proceeding, pp. 1–14). College Station, TX: Texas A&M University (TAMU).

Rebesco, M., Camerlenghi, A., & Llopart, J. (2015). Glacigenic debris flow deposits, Storfjorden Fan. In J. A. Dowdeswell, et al. (Eds.), *Atlas of Submarine Glacial Landforms: Modern, Quaternary and Ancient*. London: Geological Society, London, Special Publications, p. accepted.

Rebesco, M., Laberg, J. S., Pedrosa, M. T., Camerlenghi, A., Lucchi, R. G., Zgur, F., & Wardell, N. (2014). Onset and growth of Trough-Mouth Fans on the North-Western Barents Sea margin – implications for the evolution of the Barents Sea/Svalbard Ice Sheet. *Quaternary Science Reviews*, *92*, 227–234. Elsevier Ltd. https://doi.org/10.1016/j.quascirev.2013.08.015

Rebesco, M., Liu, Y., Camerlenghi, A., Winsborrow, M., Laberg, J. S., Caburlotto, A., … Tomini, I. (2011). Deglaciation of the western margin of the Barents Sea Ice Sheet — A swath bathymetric and sub-bottom seismic study from the Kveithola Trough. *Marine Geology*, *279*(1–4), 141–147. https://doi.org/10.1016/j.margeo.2010.10.018

Rebesco, M., Pedrosa, M. T., Camerlenghi, A., G, R., Sauli, C., Mol, B. De., … Böhm, G. (2012) One million years of climatic generated

landslide events on the northwestern Barents Sea continental margin. In Y. Yamada et al. (eds) *Submarine Mass Movements and Their Consequences, Advances in Natural and Technological Hazards Research 31* (pp. 747–756). Dordrecht, the Netherlands: Springer. https://doi.org/10.1007/978-94-007-2162-3_66

Rebesco, M., Wåhlin, A., Laberg, J. S., Schauer, U., Beszczynska-Möller, A., Lucchi, R. G., … Diviacco, P. (2013). 'Quaternary contourite drifts of the Western Spitsbergen margin. *Deep Sea Research Part I: Oceanographic Research Papers*, *79*, 156–168. Elsevier. https://doi.org/10.1016/j.dsr.2013.05.013

Rohling, E. J., Foster, G. L., Grant, K. M., Marino, G., Roberts, A. P., Tamisiea, M. E., & Williams, F. (2014). Sea-level and deep-sea-temperature variability over the past 5.3 million years. *Nature*, *508*(7497), 477–482. https://doi.org/10.1038/nature13230

Sættem, J., Bugge, T., Fanavoll, S., Goll, R. M., Mork, A., Mork, M. B. E., … Verdenius, J. G. (1994). Marine Cenozoic margin development and erosion of the Barents Sea: Core evidence from southwest of Bjornoya. *Marine Geology*, *118*, 257–281. https://doi.org/10.1016/0025-3227(94)90087-6

Sejrup, H. P., Hjelstuen, B. O., Dahlgren, K. I. T., Haflidason, H., Kuijpers, A., Nygård, A., … Vorren, T. O. (2005). Pleistocene glacial history of the NW European continental margin. *Marine and Petroleum Geology*, *22*(9–10), 1111–1129. https://doi.org/10.1016/j.marpetgeo.2004.09.007

Solheim, A., Andersen, E. S., Elverhøi, A., & Fiedler, A. (1996). Late Cenozoic depositional history of the western Svalbard continental shelf, controlled by subsidence and climate. *Global and Planetary Change*, *12*, 135–148. https://doi.org/10.1016/0921-8181(95)00016-X

Stein, R. (2008). Glacio-marine sedimentary processes. *Marine Geology*, *2*, 87–132.

Stigall, J., & Dugan, B. (2010). Overpressure and earthquake initiated slope failure in the Ursa region, northern Gulf of Mexico. *Journal of Geophysical Research*, *115*, 1–11. https://doi.org/10.1029/2009JB006848

Sultan, N., Cochonat, P., Foucher, J. P., & Mienert, J. (2004). Effect of gas hydrates melting on seafloor slope instability. *Marine Geology*, *213*(1–4), 379–401. https://doi.org/10.1016/j.margeo.2004.10.015

Svendsen, J. I., Alexanderson, H., Astakhov, V. I., Demidov, I., Dowdeswell, J. A., Funder, S., … Stein, R. (2004). Late Quaternary ice sheet history of northern Eurasia. *Quaternary Science Reviews*, *23*(11–13), 1229–1271. https://doi.org/10.1016/j.quascirev.2003.12.008

Talwani, M., & Eldholm, O. (1977). Evolution of the Norwegian-Greenland sea. *Geological Society of America Bulletin*, *88*(7), 969–999. https://doi.org/10.1130/0016-7606(1977) 88<969

Taylor, J., Dowdeswell, J. A., Kenyon, N. H., & Cofaigh, O. C. (2002). Late Quaternary architecture of trough-mouth fans: Debris flows and suspended sediments on the Norwegian margin. In J. A. Dowdeswell & Ó. C. Cofaigh (eds) *Geological Society, London, Special Publications* (pp. 55–71). London: Geological Society, London, Special Publications. https://doi.org/10.1144/gsl.sp.2002.203.01.04

Tulaczyk, S., Kamb, W. B., & Engelhardt, H. F. (2000). Basal mechanics of Ice Stream B, west Antarctica: 1. Till mechanics. *Journal of Geophysical Research*, *105*, 463. https://doi.org/10.1029/1999jb900329

Urgeles, R., Locat, J., Sawyer, D. E., Flemings, P. B., Dugan, B., & Binh, N. T. T. (2010). History of Pore Pressure Build Up and Slope Instability in Mud-Dominated Sediments of Ursa Basin, Gulf of Mexico Continental Slope. In D. C. Mosher et al. (Ed.), *Submarine Mass Movements and Their Consequences, Advances in Natural and Technological Hazards Research, 28* (pp. 179–190). Dordrecht, the Netherlands: Spinger.

Urlaub, M. (2013) *The role of sedimentation rate on the stability of low gradient submarine continental slopes, Social Sciences*. Southampton: University of Southampton.

Urlaub, M., Talling, P. J., & Masson, D. G. (2013). Timing and frequency of large submarine landslides: Implications for understanding triggers and future geohazard. *Quaternary Science Reviews*, *72*, 63–82. https://doi.org/10.1016/j.quascirev.2013.04.020

Van Hinte, J. E. (1978). Geohistory analysis: Application of micropaleontology in exploration geology. *AAPG Bulletin. American Association of Petroleum Geologists (AAPG)*, *62*(2), 201–222.

Vanneste, M., Heureux, J. L., Baeten, N., Brendryen, J., Vardy, M. E., Steiner, A., … Reichel, T. (2012). Shallow landslides and their dynamics in coastal and deepwater environments, Norway. In Y. Yamada et al. (Eds.), *Submarine Mass Movements and Their Consequences, Advances in Natural and Technological Hazards Research 31* (pp. 29–41). Dordrecht, the Netherlands: Springer. https://doi.org/10.1007/978-94-007-2162-3

Vorren, T. O., & Laberg, J. S. (1997). Trough Mouth Fans - Paleoclimate and ice-sheet monitors. *Quaternary Science Reviews*, *16*(97), 865–881. https://doi.org/10.1016/S0277-3791(97)00003-6

Vorren, T. O., Lebesbye, E., & Larsen, K. B. (1990). Geometry and genesis of the glacigenic sediments in the southern Barents Sea. In J. A. Dowdeswell & J. D. Scourse (Eds.), *Glacimarine environments: Processes and sediments*. *Special pu. London: Geological Society*, pp. 269–288. https://doi.org/10.1144/gsl.sp.1990.053.01.15

SUPPORTING INFORMATION

Additional supporting information may be found online in the Supporting Information section at the end of the article.

How to cite this article: Llopart J, Urgeles R, Forsberg CF, et al. Fluid flow and pore pressure development throughout the evolution of a trough mouth fan, western Barents Sea. *Basin Res*. 2019;31:487–513. https://doi.org/10.1111/bre.12331